

2
857
OG
m68
2006

2-D KASAI VELOCITY ESTIMATION FOR DOPPLER OPTICAL COHERENCE TOMOGRAPHY

by

Darren Morofke, B.Eng

Ryerson University

Toronto, Ontario, Canada, 2004

A thesis

presented to Ryerson University

in partial fulfillment of the

requirement for the degree of

~~Masters~~ of Applied Science

in the Program of

Electrical and Computer Engineering

Toronto, Ontario, Canada, 2006

© Darren Morofke 2006

PROPERTY OF
RYERSON UNIVERSITY LIBRARY

UMI Number: EC53526

INFORMATION TO USERS

The quality of this reproduction is dependent upon the quality of the copy submitted. Broken or indistinct print, colored or poor quality illustrations and photographs, print bleed-through, substandard margins, and improper alignment can adversely affect reproduction.

In the unlikely event that the author did not send a complete manuscript and there are missing pages, these will be noted. Also, if unauthorized copyright material had to be removed, a note will indicate the deletion.



UMI Microform EC53526
Copyright 2009 by ProQuest LLC
All rights reserved. This microform edition is protected against
unauthorized copying under Title 17, United States Code.

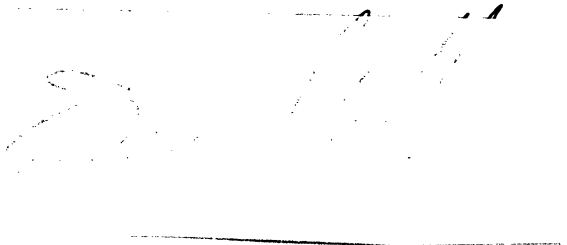
ProQuest LLC
789 East Eisenhower Parkway
P.O. Box 1346
Ann Arbor, MI 48106-1346

AUTHOR'S DECLARATION

I, Darren Morofke, hereby declare that I am the sole author of this thesis.

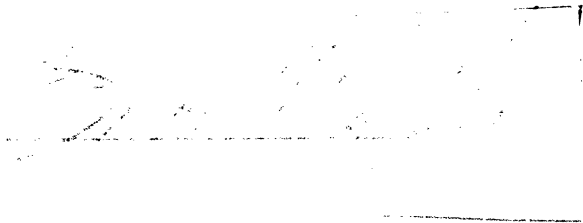
I authorize Ryerson University to lend this thesis to other institutions or individuals for the purpose of scholarly research.

* Signature

A handwritten signature in dark ink, appearing to read 'Darren Morofke', is written over a faint rectangular box.

I further authorize Ryerson University to reproduce this thesis by photocopying or by other means, in total or in part, at the request of other institutions or individuals for the purpose of scholarly research.

* Signature

A second handwritten signature in dark ink, appearing to read 'Darren Morofke', is written over a faint rectangular box.

*The Author's Declaration Page must be signed in the two locations prior to the thesis being submitted to the School of Graduate Studies.

BORROWER'S PAGE

ABSTRACT

2-D KASAI VELOCITY ESTIMATION FOR DOPPLER OPTICAL COHERENCE TOMOGRAPHY

Darren Morofke, Master of Applied Science, 2006

Department of Electrical and Computer Engineering, Ryerson University

Optical Coherence Tomography (OCT) is a high-resolution, non-invasive technique to image subsurface tissue and tissue functions. A broadband light source illuminates an object and the reflected photons are processed using an interferometer, demodulated into inphase and quadrature components and then digitized. The captured data contains information about the velocity of the moving scatterers but current Doppler estimation algorithms have a limited velocity detection range. Here we demonstrate Doppler OCT (DOCT) detection of *in vivo* of blood flow in a rat aorta with over 1 m/s peak velocity through an esophageal DOCT probe using a new processing technique. Previous methods have used a transverse Kasai (TK) autocorrelation estimation to estimate the velocity. By calculating the Kasai autocorrelation with a lag in the depth or axial direction, backscattered frequency information is obtained. Through subtraction with stationary backscattered information, the Doppler shift is obtained by the axial Kasai (AK) technique. Maximum non-aliased Doppler frequency estimation using a time domain DOCT system increased from ± 4 kHz to ± 1.6 MHz. The TK has better velocity resolution in the low flow rate range and when combined with the AK we demonstrate a dynamic frequency range over 100 dB with a velocity detection range from 10 $\mu\text{m/s}$ to over 1 m/s. This velocity range spans from microcirculation to cardiac blood flow velocities.

ACKNOWLEDGEMENTS

First I would like to thank my two supervisors: Dr. Mike Kolios and Dr. Victor Yang for their hard work at making me work even harder. If it wasn't for Mike's weekly meetings and Victor's insight, this project would not have been possible. I would also like to thank Adrian for his help in Matlab / Thorlabs and Beau for his tutoring with the old but reliable time domain OCT system that was used for the this thesis. I would like to thank my undergraduate supervisor, Dr. Kaamram Raahemifar for making me believe that I was capable of more.

I would also like to thank my father, mother and Jessica for their support and motivation.

DEDICATION

To the people that helped me to not choose the path of least resistance.

TABLE OF CONTENTS

AUTHOR'S DECLARATION	II
BORROWER'S PAGE.....	III
ABSTRACT.....	IV
ACKNOWLEDGEMENTS	V
DEDICATION	VI
TABLE OF CONTENTS	VII
LIST OF TABLES.....	IX
LIST OF FIGURES AND ILLUSTRATIONS.....	X
LIST OF FIGURES AND ILLUSTRATIONS.....	X
CHAPTER 1: INTRODUCTION AND BACKGROUND.....	- 1 -
1.1 INTRODUCTION	- 1 -
1.2 THESIS ORGANIZATION	- 1 -
1.3 MEDICAL IMAGING BACKGROUND	- 3 -
1.3.1 OCT Imaging Modes.....	- 4 -
1.3.2 Biological Background	- 6 -
1.4 FLUID DYNAMICS	- 7 -
1.4.1 Reynolds Numbers	- 8 -
1.4.2 Flow Velocity and Profile	- 8 -
1.4.3 Junction Distances	- 9 -
1.5 DOPPLER EFFECT	- 10 -
1.6 LASERS AND OPTICS	- 13 -
1.6.1 Refraction.....	- 13 -
1.6.2 Michelson interferometer.....	- 14 -
1.6.3 Fourier Domain Rapid Scanning Optical Delay Line (RSOD).....	- 16 -
1.7 SIGNAL SAMPLING AND PROCESSING	- 18 -
1.7.1 Sampling Theorem and Aliasing.....	- 19 -
1.7.2 In-Phase and Quadrature Demodulation.....	- 20 -
1.8 OCT	- 22 -
1.8.1 Resolution Limits of OCT.....	- 23 -
1.9 OCT VERSUS ULTRASOUND	- 26 -
2 CHAPTER 2: METHODS.....	- 27 -

2.1	PHASE BASED VELOCITY ESTIMATION TECHNIQUES.....	- 27 -
2.2	KASAI AUTOCORRELATION ESTIMATION.....	- 28 -
2.3	TRANSVERSE KASAI AUTOCORRELATION ESTIMATE.....	- 31 -
2.4	PROPOSED ALGORITHM: THE AXIAL KASAI	- 32 -
3	CHAPTER 3: EXPERIMENTS AND RESULTS	- 35 -
3.1	EXPERIMENT 1 – GRAVITY FED FLOW PHANTOM.....	- 35 -
3.1.1	<i>Angle</i>	- 37 -
3.1.2	<i>Experimental Flow measurement</i>	- 38 -
3.1.3	<i>Low-Flow Experimental Observations</i>	- 39 -
3.2	EXPERIMENT 2 – WIDE RANGE OF FLOW	- 41 -
3.3	EXPERIMENT 3 – <i>IN VIVO</i> ANIMAL EXPERIMENTATION.....	- 47 -
4	CHAPTER 4: CONCLUSION	- 51 -
4.1	FUTURE WORK	- 52 -
4.2	FUNDING	- 53 -
	REFERENCES	1
B	LIST OF SYMBOLS.....	3

LIST OF TABLES

Table 4.1 – Experimental Parameters	- 39 -
---	--------

LIST OF FIGURES AND ILLUSTRATIONS

Figure 1.1 – Example of B-Mode and M-Mode images. A) The sweeping motion of the probe to acquire the scan is shown while B) and C) are structural and Doppler B-Mode images from the scan. B-Mode image is a 1.5 mm x 1.5 mm square. D) The static recording of an M-Mode image through the centre of the tube. E) and F) show structural and Doppler M-Mode images. M-Mode images have a depth of 1.5 mm and span 1/8 th of a second. Vessel contains 1% Intralipid fluid moving at 1.5 mm/s peak velocity.	4 -
Figure 1.2 – Human blood circulation map [5].	7 -
Figure 1.3 – How a parabolic velocity profile develops after a tube diameter change in the worst cast scenario of a flat flow profile.	9 -
Figure 1.4 – Doppler Shift experienced by a moving car. Car is playing trendy music containing only one frequency, f_o . Doppler shift would cause Person 1 would hear to hear a $+f_D$ frequency shift while Person 2 would hear a $-f_D$ frequency shift.	11 -
Figure 1.5 – Visual representation of Doppler angle θ assuming no change in angle due to index of refraction.	12 -
Figure 1.6 – Refraction occurring as light passes from air in glass vessel carrying Intralipid solution, note the doppler angle of 45° is bent to 58°.	14 -
Figure 1.7 – Diagram of a Michelson interferometer.	15 -
Figure 1.8 – Theoretical interference pattern from Michelson Interferometer using a broadband light source of 1.3 μm with 60 nm of bandwidth in Intralipid solution with $n=1.33$. Distance peaks is 0.49 μm due to the refractive index of Intralipid.	16 -
Figure 1.9 – Fourier domain Rapid Scanning Optical Delay Line (RSOD).	18 -
Figure 1.10 – Example of under sampling, the line is the signal while the dots represent the sampled data.	19 -
Figure 1.11 – Example of reference signal being compared to the measured signal. Courtesy of Victor Yang.	21 -
Figure 1.12 – Block Diagram of in-phase and quadrature demodulation. BPD Balanced Photo Detector; AMP Trans-impedance amplifier; HPF High Pass Filter; LPF Low pass filter.	21 -
Figure 1.13 – LS: light source; PC: polarization controller; OC: optical circulator; 3 dB: 50-50 fiber coupler; PM: phase modulator; RSOD: rapid scanning optical delay line; BPD:	

balanced photo-detector; PMD: phase modulator driver; I&Q: inphase and quadrature demodulator; SD-1 & 2: scanner drivers; COMP: computer.....	23 -
Figure 1.14 – Beam profiles for low and high numerical aperture showing relationship between depth and transverse resolution.....	24 -
Figure 1.15 – Axial resolution versus bandwidth. Light with a 1.3 μm and 60 nm BW is highlighted.	25 -
Figure 1.16 – Data courtesy of A.W. Sainter, T.A. King, M.R. Dickinson [13] represents the attenuation versus wavelength while The first peak depth penetration occurs at ~ 1400 nm...-	25 -
Figure 2.1 – Example of TK estimation between two pulses [25].....	32 -
Figure 3.1 – Diagram of the gravity flow setup.	36 -
Figure 3.2 – Picture of experimental gravity pump setup.	37 -
Figure 3.3 – Experimental Apparatus with a Doppler angle of 86°	38 -
Figure 3.4 – Select flow profiles demonstrating accuracy of TK estimate. A) slow flow B) flow at half velocity detection at this angle C) Flow causing 1 aliasing ring D) flow causing 2 aliasing rings.	40 -
Figure 3.5 – Digital picture of experimental setup A) medical infusion pump B) picture of probe mounted to a scanning reference arm, probe can be seen on the bottom of the reference arm.	41 -
Figure 3.6 – (A) Change in the AK estimated frequency as a function of flow velocity. When no-flow AK (solid line) result subtracted from the flowing channels, a family of parabolic shapes is obtained (B); Positively labeled velocities indicate flow towards the detector, negative velocities are away. Peak flow velocities are +34, +20, +11, no flow, -11, -19, -25, -34, -43 and -57 cm/s from top to bottom.	42 -
Figure 3.7 - TK and AK estimated peak velocities are compared to experimental peak velocities. (A) Peak velocities derived from TK and AK algorithms recorded over a large range of velocities. (B) A detailed view of TK shifts for lower flows. Error bars are result of standard error. The solid line is the line of identity.	43 -
Figure 3.8 – Ultrafast M-Mode flow image. A) Structural image range 6dB to 72dB. B) TK range -4 kHz to 4kHz. C) AK range 2 MHz to 2 MHz. When the Doppler shift increases to 1800 kHz that the signal begins to vanish in all three images as predicted.....	44 -
Figure 3.9 – Contour map of error versus a change in N and M. $N=M=32$ is highlighted.....	44 -

- Figure 3.10 - M-mode images of the three detection zones showing structural, AK and TK renderings. In zone I, TK accurately measures velocity, and the aliasing rings in zone II can be unwrapped reliably. In zone III, the aliasing rings on the TK are smaller than the spatial resolution of the system and can not be accurately unwrapped. The AK is able to accurately measure flow in zone III, but not in zones I and II.- 46 -
- Figure 3.11 – AK velocity estimation for two different angles. Estimation corrected for refraction and angle.....- 47 -
- Figure 3.12 –Schematics of the mechanical assembly for the linear scanning catheter, courtesy of Victor Yang. A) Top-view. B) Side-view.....- 48 -
- Figure 3.13 – Schematic of the EDOCT catheter distal end, courtesy of Victor Yang. A) Fiber termination with a GRIN lens and right angle prism. The terminated fiber can slide within either a steel cap, with the optical beam passing through one of the slots B) or within a transparent plastic cover seen in C).- 48 -
- Figure 3.14 – *In-vivo* images of trans-esophageal Doppler OCT of rat aortic blood flow. (A) TK results overlaid on structural image. Doppler signals indicate aortic wall motion (*), systolic rush of high-speed blood flow (**), and regions of slow flow between heart beats (white arrows). (B) AK results overlaid on the same structural image, with the esophagus and aortic wall labelled. High speed systolic flow regions consistent with large Doppler frequency shifts are clearly visualized. The temporal flow profiles measured at the dotted lines of corresponding colors in (B) are plotted in (C).- 50 -

1 Chapter 1: Introduction and Background

Optical Coherence Tomography (OCT) is a high-resolution, non-invasive imaging modality that can image subsurface tissue structure and functions [1]. This thesis project describes the application of a new velocity estimation method through the calculation of the Doppler frequency shift using an autocorrelation mean frequency estimator. This new algorithm allows for a velocity detection range that is usable in cardiac applications.

1.1 Introduction

The field of medical imaging impacts the lives of most Canadians. People in the field are familiar with clinically established imaging techniques such as ultrasound, X-Ray, MRI and CT. OCT is a new imaging modality that has great promise for non-invasive sub-surface imaging at a resolution approaching that of optical microscopy which is used for histology analysis. This could potentially be used to detect diseases such as cancer *in vivo* and in real time. Sometimes referred to as ultrasound with light, OCT has similarities in signal processing algorithms to its acoustic counterpart. The system used [2] utilized the Kasai autocorrelation method for velocity estimation, but was limited in its detection range. Increasing this range became the subject of my research.

1.2 Thesis Organization

The rest of the chapters of this thesis are organized as the following. Chapter 1 gives the reader a brief background in medical imaging and a biological perspective. Since the project deals with flow rates and velocity estimation, the basics of fluid dynamics are discussed including a section on the Doppler effect. This is followed by a review of basic optical principles, interferometer

theory, modulation methods and aliasing issues along with the effects on velocity estimation. Segments from these previous sections are tied together in the OCT theory section so that the reader is given an appreciation of the general principles behind this imaging modality.

The mathematical derivation of the autocorrelational methods used for flow detection are described in Chapter 2. Detailing past and present generation Kasai autocorrelation estimation methods with applications to ultrasound and OCT, the proposed variant used to extend the velocity range is explained. It is shown that the axial Kasai estimation estimates the mean backscattered carrier frequency, and thus the remaining frequency after background subtraction is the Doppler effect.

In chapter 3, the experiments designed to test the velocity estimation algorithms are described. To test the ability to measure flow in a controlled environment, an artificial flow phantom setup was filled with Intralipid to model steady state flow through a capillary via imaging of a 0.5 mm inner diameter glass vessel. This algorithm was further tested using *in vivo* endoscopic DOCT data from male Fischer rats. Two methods were used for the flow phantom setups. One was a gravity fed system while the other was driven with a medical infusion pump. The experimental data is shown graphically, in images and the specifications are outlined.

Conclusions and future work are presented in Chapter 4. The impact of the findings presented in the thesis are discussed and potential future projects and applications that can be derived from the findings of this research project are outlined. Finally, there is a preview of some preliminary data suggesting spectroscopic applications for the AK when applied to OCT.

1.3 Medical Imaging Background

Robert Hooke used microscopes to discover and study the human cell in 1665. Since then, imaging methods have been developed with a resolution of 10 angstroms using a scanning electron microscope, which is a $\sim 2,000,000\times$ magnification [3]. Ultrahigh resolution modalities like this can not be used *in vivo* because they require the sample to be in an environment that would not be favourable to the conditions of life.

The advancement of diagnostic imaging of humans has been developed during the past 120 years with the discovery X-ray's in 1895 by Wilhelm Röntgen [4]. The simple X-ray has been advanced by modern computers and 3D images that can be generated through computer tomography (CT). These methods are able to image skeletal structures but their ability to visualize soft tissue is poor. X-ray's spatial resolution is roughly 0.1 mm. Magnetic Resonance Imaging (MRI) has exceptional soft tissue visualization abilities. MRI imaging systems have a spatial resolution of roughly 0.5 mm and are the most expensive and technologically complex of the imaging modalities. A less expensive imaging technique that has some soft tissue contrast is ultrasound imaging. This modality is used in standard clinical practice and is capable of resolutions between 0.1 mm and 1 mm. High frequency ultrasound can obtain a resolution from 10 μm to 100 μm at the expense of penetration depth.

Sometimes referred to as ultrasound with light, Optical Coherence Tomography (OCT) uses some of the same signal processing techniques as ultrasound and generates images with similar speckle patterns. Technologically, however, OCT is more complex than ultrasound. OCT has a resolution approaching that of methods used for histology, or between 1 μm and 10 μm . What

sets OCT apart from other ultrahigh resolution imaging techniques is that it is able to achieve high penetration depths for its resolution characteristics. While confocal microscopy is only able to obtain 100 – 200 μm depth penetration, OCT has been shown to have a depth of 2 mm in non-transparent tissue structures such as human skin.

1.3.1 OCT Imaging Modes

In OCT, the image is generated by the rotation of a single laser beam through a given angle. Through interferometer techniques, discussed in chapter 1.6.2, depth information can be isolated along the path of the beam. The depth information resolved along one complete line is referred to as an axial-scan (a-scan) and contains a single dimension, depth.

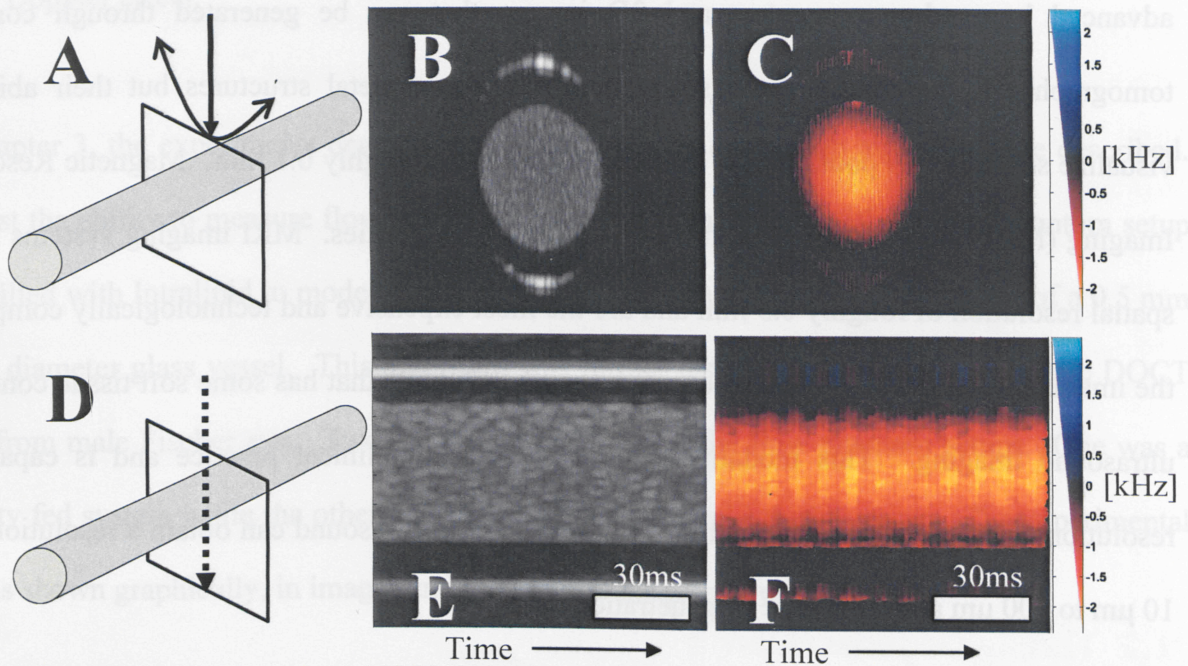


Figure 1.1 – Example of B-Mode and M-Mode images. A) The sweeping motion of the probe to acquire the scan is shown while B) and C) are structural and Doppler B-Mode images from the scan. B-Mode image is a 1.5 mm x 1.5 mm square. D) The static recording of an M-Mode image through the centre of the tube. E) and F) show structural and Doppler M-Mode images. M-Mode images have a depth of 1.5 mm and span 1/8th of a second. Vessel contains 1% Intralipid fluid moving at 1.5 mm/s peak velocity.

Two image modes extensively detailed in this thesis are M-Mode and B-Mode. They are similar to the corresponding modes for ultrasound. Both modes contain depth information but in

M-Mode a constant location (depth) is varied across time while the B-Mode translates the probe through a fixed angle on a pivot making the second dimension a transverse position. Both methods consist of a number of complete axial scans (a-scans) which are stacked beside each other to obtain their second dimension.

Data for an M-Mode image is acquired by combining multiple a-scans from the same transverse location over time. The separation between the same depth on two adjacent a-scans is $\frac{1}{f_a}$ or 0.125 ms on this system. The a-scans are stacked together in a 2D-image with the x-axis corresponding to time and the y-axis corresponding to depth. This imaging format is very useful for applications where temporal dynamics are important, such as observing blood flow through the heart valves and chambers. Figure 1.1 shows the schematic of an M-Mode scan (D), the corresponding structural image (E) and Doppler shift image (F). As with the Doppler B-Mode image the peak velocity occurs, as predicted for parabolic flow profiles, in the centre of the capillary. The temporal characteristics of the M-Mode image can be seen in this Doppler frequency image with the pulsation effect from motor representing as slight velocity changes.

A B-Mode image is constructed by assembling a number of a-scans for sequentially spaced locations in the transverse direction. OCT imaging systems rotate the probe on a fixed pivot point through a small angle which relates to a change in physical location. The images generated for this mode are in two-dimensional space with depth (μm) plotted against transverse location (μm). Since the angle of rotation is so small the non-linear nature from the curvature of the scan is barely noticeable. Figure 1.1A shows a diagram illustrating the capture and display of a B-Mode image and the corresponding structural (B) and calculated Doppler frequencies (C). Note

that the peak of the frequency shift occurs, as expected for parabolic flow, in the centre of the tube.

Different types of quantitative data can be displayed in an M-Mode or B-Mode image. Structural data displays intensity of the backscattered light, which is related to the reflectivity of the sample. Since the intensity of the reflected light rapidly decays due to scattering and absorption, it is plotted on a logarithmic scale in decibels (dB). The structural images in this thesis are plotted using a grayscale colour map which represents the backscattered intensity as a function of color. The lower limit on the colour map occurs for signals less than 6 dB represented by a black while signals greater than 72 dB are represented by white. Doppler shifts are presented as frequency estimated with black being '0', red and yellow for negative frequencies, and blue and light blue representing positive frequencies. The frequency range displayed can change from image to image and will be shown on the image or mentioned in the caption. The Doppler frequency directly relates to the estimated velocity by a formula, as explained later in the fluid dynamics section. Flow through a tube is assumed to be parabolic given the experimental conditions.

1.3.2 Biological Background

The human body is a complex system containing a vast network of interlinking blood lines carrying blood towards or away from the heart. The heart is able to produce a flow rate up to 4 L/minute with a peak velocity of 20 m/s. In contrast, the aorta of a rat is roughly 1.5 mm in diameter and has flow velocities ranging from 87 cm/s to over 5 m/s [6]. The network of veins and arteries in a human can be seen in Figure 1.2. Linking off of these are smaller vessels such as arterioles and venules. Arterioles are as small as 10 μm with flow velocities less than 1.5

mm/s. Venules are larger structures and have diameters ranging from 10 - 200 μm with blood velocities between 2 - 3 mm/s.

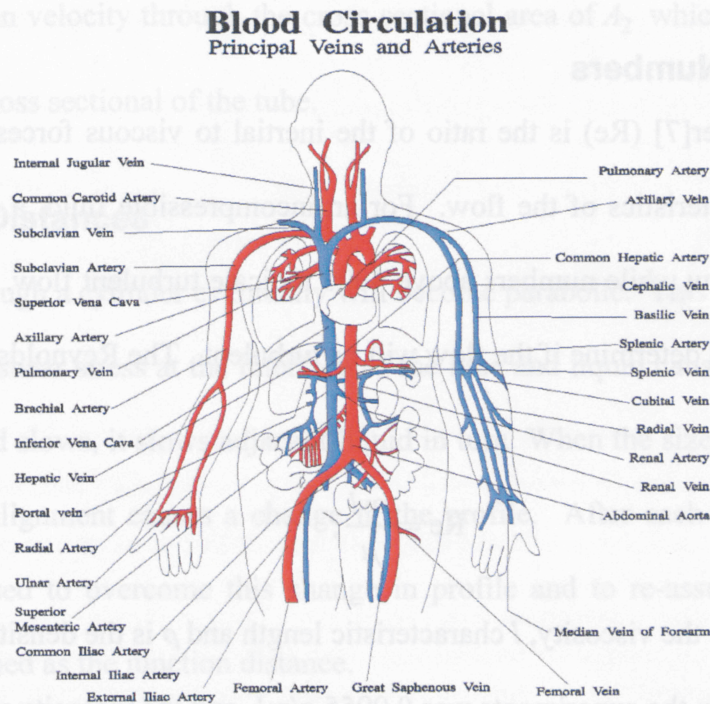


Figure 1.2 – Human blood circulation map [5].

Human blood cells are roughly 7 μm in diameter and 2 μm in thickness, which means that on an OCT system one is almost able to resolve individual cells. Because of the 1-10 μm resolution on OCT, it is an ideal tool for non-invasively measuring the flow rates in the microcirculation. This is useful to detect the growth of new blood vessels, called angiogenesis. Angiogenesis occurs when there is an increase of blood to an area which is injured, or more importantly when a tumor is growing.

1.4 Fluid Dynamics

A flow of liquid can be either laminar or turbulent. Laminar flow is smooth steady flow which occurs in parallel layers. Laminar flow through a cylinder is characterized by a parabolic velocity profile with the peak velocity occurring in the centre of the vessel and no motion at the

interface of the wall. This flow becomes parabolic after a specific junction distance. Turbulent flow is chaotic, stochastic and difficult to accurately model.

1.4.1 Reynolds Numbers

The Reynolds number[7] (Re) is the ratio of the inertial to viscous forces, and can be used to determine the characteristics of the flow. For an incompressible fluid, a Re of less than 2200 ensures a laminar flow while numbers above 4000 indicate turbulent flow. In the middle range, other factors are used determine if the flow will be turbulent. The Reynolds number is calculated as,

$$\text{Re} = \frac{\rho v l}{\mu}, \quad (1.1)$$

where v is velocity, μ the viscosity, l characteristic length and ρ is the density. The density of 1% Intralipid fluid used in the experiments was 0.9955 g/mL and the viscosity was 1.36 cP.

1.4.2 Flow Velocity and Profile

Under laminar flow condition, fluid flows in smooth lines and has a predictable flow profile. Assuming laminar flow through a long rigid tube, a parabolic velocity profile is obtained if the Re is less than 2200. Given these assumptions the velocity profile is given by,

$$v(r) = \left(1 - \frac{r^2}{R^2}\right) v_o, \quad (1.2)$$

where v_o is the velocity at the centre of the vessel, R is the radius of the vessel and r is the radial position. When laminar flow is assumed the maximum velocity in the centre of the tube is,

$$v_o = 2 \frac{A_2 \bar{v}_2}{A_1}, \quad (1.3)$$

where \bar{v}_2 is the mean velocity through the cross sectional area of A_2 which is equal to the flow rate, and A_1 is the cross sectional of the tube.

1.4.3 Junction Distances

A constant flow through a cylinder eventually will become parabolic. This profile exists because there is the greatest shear stress at the interface of the tube and liquid causing the liquid to slow down. As this liquid slows, it slows adjacent liquid in turn. When the size of a tube is changed, turbulence and misalignment causes a change in the profile. After each junction, a minimum length must be passed to overcome this change in profile and to re-assume a parabolic flow profile. This is defined as the junction distance.

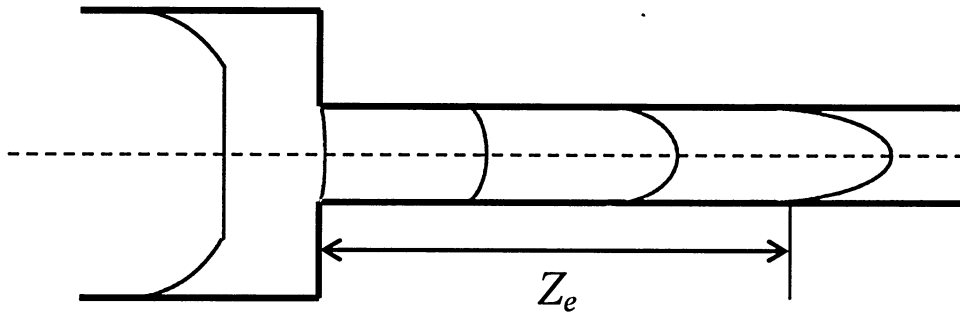


Figure 1.3 – How a parabolic velocity profile develops after a tube diameter change in the worst cast scenario of a flat flow profile.

Assuming a flat velocity profile at the junction the entrance length is defined as:

$$Z_e = \frac{R \cdot R_e}{15}, \quad (1.4)$$

where Z_e is the distance between the junction and the location the parabolic flow profile begins, R is the radius of the tube and R_e is the Reynolds number for the fluid. When this length has been surpassed, the flow profile has a parabolic shape. However, in most circumstances, the incoming profile is already partly parabolic and so this entrance effect is considered to be a worst case scenario.

1.5 Doppler Effect

The Doppler effect is defined as a compression or an expansion of an incident waveform caused by motion. This is visually represented in Figure 1.4. The car moving towards person 1 causes a compression of the sound wave, thus increasing the audible frequency whereas sound waves received by person 2 are expanded causing a decrease in frequency. This change in frequency is based on the velocity change between the receiver and the emitter as,

$$\begin{aligned} f &= f_o + f_D \\ f_D &= \frac{v_{rel}}{v} f_o, \end{aligned} \quad (1.5)$$

where f is the new frequency, f_o is the original frequency, f_D is the Doppler frequency, v_{rel} is the relative velocity between the emitter and the receiver and v is the velocity of the wave in the medium.

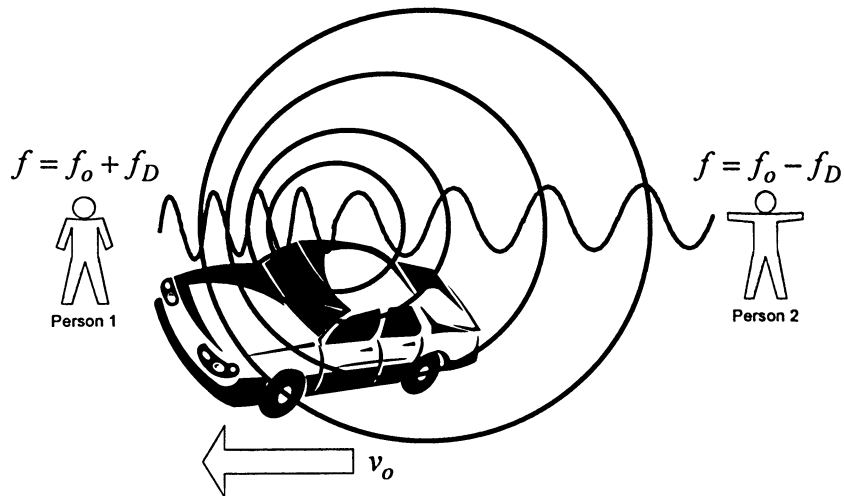


Figure 1.4 – Doppler Shift experienced by a moving car. Car is playing trendy music containing only one frequency, f_o . Doppler shift would cause Person 1 would hear to hear a $+f_D$ frequency shift while Person 2 would hear a $-f_D$ frequency shift.

Light waves experience a similar phenomenon, but instead of a change in audible frequency, there is a shift in color. When a Doppler shift [8] affects visible light, it is called a red shift if the distance between the source and observer increasing or blue shift if it is decreasing.

The shift in frequency relates directly to a change in velocity and the speed of light in a medium is $\frac{c}{n}$ so a change in frequency can be related to the velocity by

$$\begin{aligned}
 f_D &= \frac{v_o}{v} f_o \\
 f_D &= \frac{v_o}{\frac{c}{n} - v_o} f_o \cong \frac{v_o}{\frac{c}{n}} f_o = \frac{v_o}{n\lambda_o}, \\
 v_o &= \frac{f_D \lambda_o}{n}
 \end{aligned} \tag{1.6}$$

where λ_o is the wavelength of the light, c is the speed of light and n is the index of refraction of the medium. However, in the case of a backscattered wave, the relationship between backscattered frequency and velocity is,

$$v = \frac{f_D \lambda_o}{2n}, \quad (1.7)$$

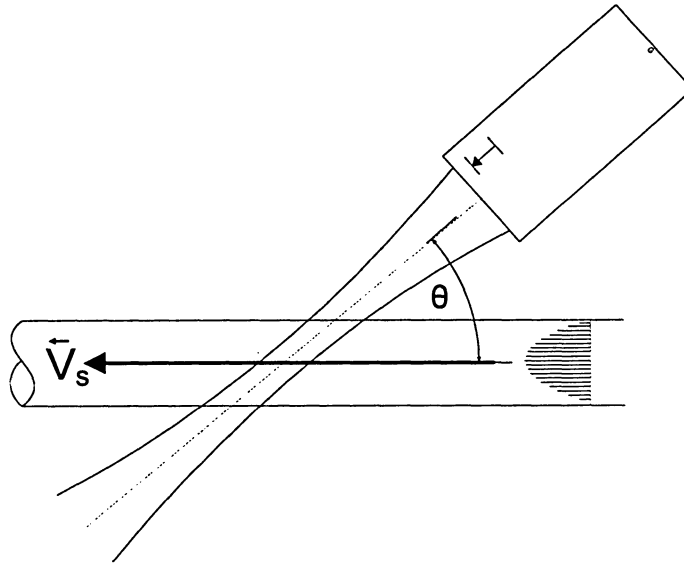


Figure 1.5 – Visual representation of Doppler angle θ assuming no change in angle due to index of refraction.

A further modification to equation with respect to Doppler angle is,

$$v = \frac{\lambda_o f_D}{2n_i \cos \theta} \quad (1.8)$$

where λ_o is the centre wavelength of the light, Δf is the frequency change and θ is the Doppler angle as defined by Figure 1.5.

1.6 Lasers and Optics

1.6.1 Refraction

Light waves change direction, as they pass from one medium to another. This effect is known as refraction and is caused by a change of velocity in the speed of light between the two mediums. A change in velocity causes the light to bend towards or away from the normal of the surface so long as the incident angle is less than the angle of total internal reflection. This effect can be described by Snells [8] law,

$$\begin{aligned} n_1 \sin \theta_1 &= n_2 \sin \theta_2 \\ \theta_2 &= \arcsin \left(\frac{n_1}{n_2} \sin \theta_1 \right), \end{aligned} \quad (1.9)$$

where n and θ are the index of refraction and incident angle from the normal the surface. This equation infers that if $n_1 < n_2$ the light will bend towards the normal but if $n_2 < n_1$ that the light will bend away. Since the laser is passing from air into another material, the bending always occurs away from the normal. The refractive index of air is 1.0003, water is ~ 1.333 , tissue is ~ 1.4 and glass is ~ 1.5 . The concentration of Intralipid fluid used in experimentation is 1% Intralipid solution and 99% water, however the index of refraction is assumed to be close to that of water or ~ 1.33 .

The effect of refraction on a laser passing from air into glass and then into a solution of Intralipid, which is the setup for the experiments, is shown in Figure 1.6.

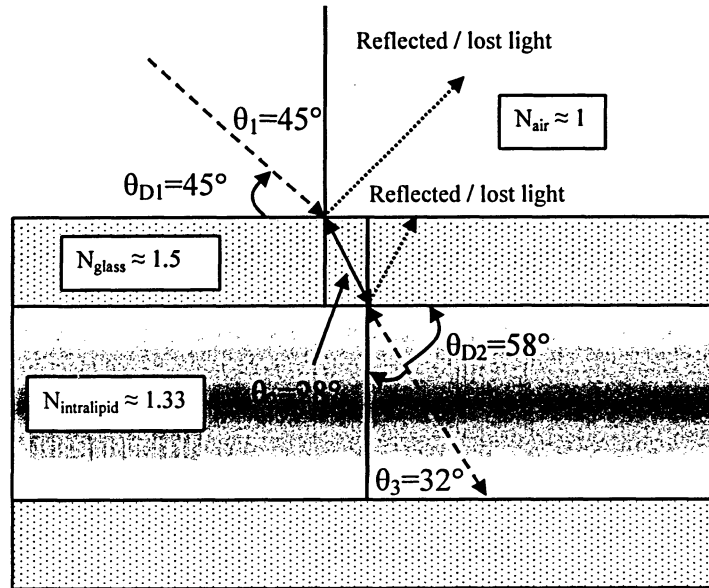


Figure 1.6 – Refraction occurring as light passes from air in glass vessel carrying Intralipid solution, note the Doppler angle of 45° is bent to 58°.

1.6.2 Michelson interferometer

The Michelson Interferometer [8-10] splits a beam of light into two parts by a beam splitter, one of which is sent to a reference arm and the other to a scattering object. Light reflected back from both the object and the reference arm re-combines at a detector. The recombination creates an interference pattern. A diagram of the Michelson Interferometer is shown in Figure 1.7. If a coherent, single frequency, light source is analyzed using an interferometer, constructive and destructive interference occur when path lengths of the light combining at the detector differ by a whole or half wavelength, respectively. The result of this is a sinusoidal pattern with maximum intensity at whole wavelength path differences and minimum intensity occurring at a half wavelength path difference. However, when a low-coherent broadband light is used, the backscattered photons have only a small coherence length in which they can constructively or destructively interfere.

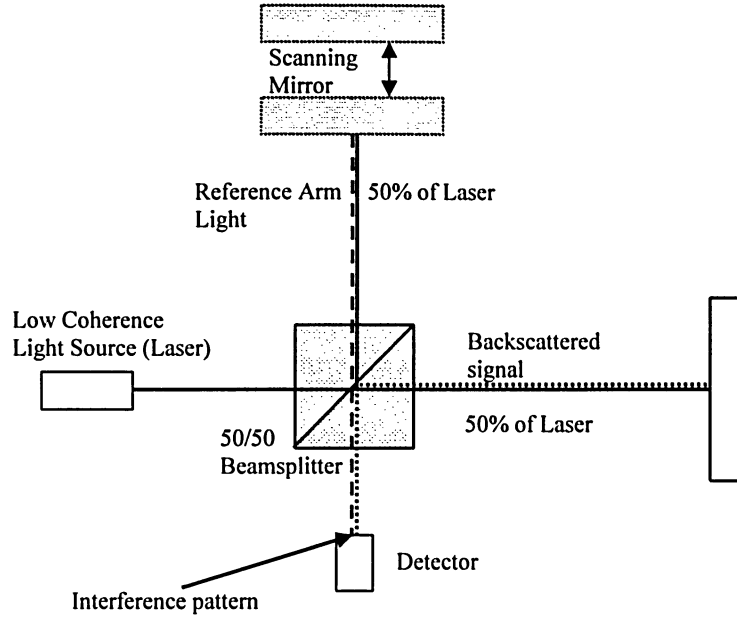


Figure 1.7 – Diagram of a Michelson interferometer.

Biological tissue is not very reflective. The interference visibility is determined by,

$$\text{Visibility} = \frac{I_{\max} - I_{\min}}{I_{\max} + I_{\min}}, \quad (1.10)$$

where I_{\max} is maximum intensity of the fringe and I_{\min} is the minimum intensity of the fringe. The typical range is for visibility is between 10^{-6} and 10^{-3} . When using coherent light, these fringes are visible through a specific coherence length. Assuming that the light source is Gaussian in its spectrum, the coherence length can be calculated as [10],

$$l_c = \frac{2 \ln 2}{\pi n} \frac{\lambda_0^2}{\Delta \lambda}, \quad (1.11)$$

where $\Delta \lambda$ is the full width half maximum (FWHM) bandwidth of the light used. The coherence length relates directly to the intensity pattern of the backscattered light. The intensity of the

backscattered light from a single scattering object has a Gaussian decay as a function of the coherence length as,

$$I(z) = I_o \left[1 + e^{-\left(\frac{z-z_o}{l_c}\right)^2} \cos\left(4\pi \frac{z-z_o}{\lambda_o}\right) \right], \quad (1.12)$$

where I is the intensity at the specific reference arm length and $z-z_o$ is the change in reference arm. The visibility versus reference arm length is shown in Figure 1.8.

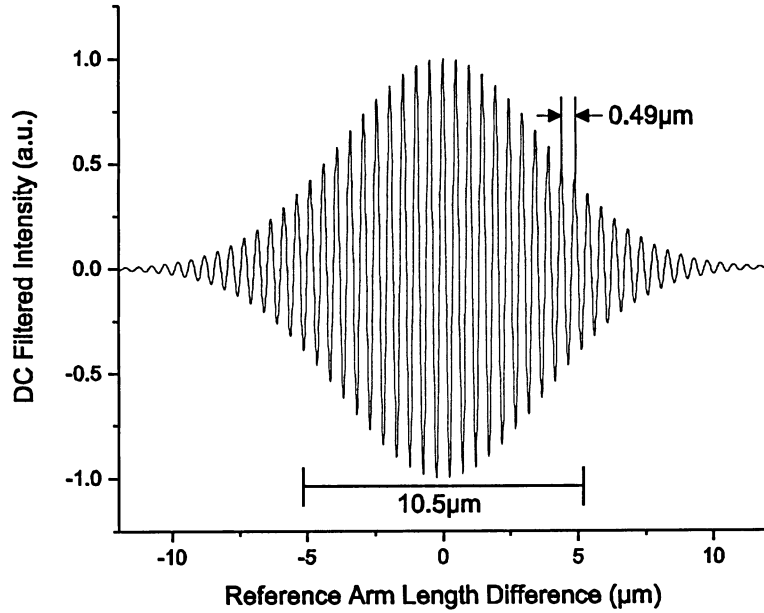


Figure 1.8 – Theoretical interference pattern from Michelson Interferometer using a broadband light source of 1.3 μm with 60 nm of bandwidth in Intralipid solution with $n=1.33$. Distance peaks is 0.49 μm due to the refractive index of Intralipid.

1.6.3 Fourier Domain Rapid Scanning Optical Delay Line (RSOD)

The Michelson interferometer is used in OCT to isolate photons for specific depths controlled by the spatial location of the mirror in the reference arm. In the original setup, the reference arm

was physically moved an equivalent distance to that of the depth in the sample. For 32 frames per second, a depth penetration of 1.5 mm and 1000 a-scans, this would require the mirror to be moving at a fixed speed of 48 m/s, or 172 km/hour through the 1.5 mm space. Even the most expensive servo motors would have a difficult time obtaining this speed over a 1.5 mm space, let alone reversing quickly enough to repeat the cycle. To overcome this limitation, a Fourier based Rapid Scanning Optical Delay (RSOD) [10, 11] was implemented. According to the Fourier transform, if a phase ramp is imparted in the spectral domain, there will be a corresponding spatial delay created in the time domain,

$$f[g(t-t_o)] = G(\omega) \cdot e^{-i\omega t_o}, \quad (1.13)$$

Broadband light that is reflected off a diffraction grating is separated into its different frequency components. This is analogous to the transform of the spatial domain into the spectral domain. To use this in OCT, a fiber optic cable carrying the broadband light source is deflected off a diffraction grating as seen in Figure 1.9.

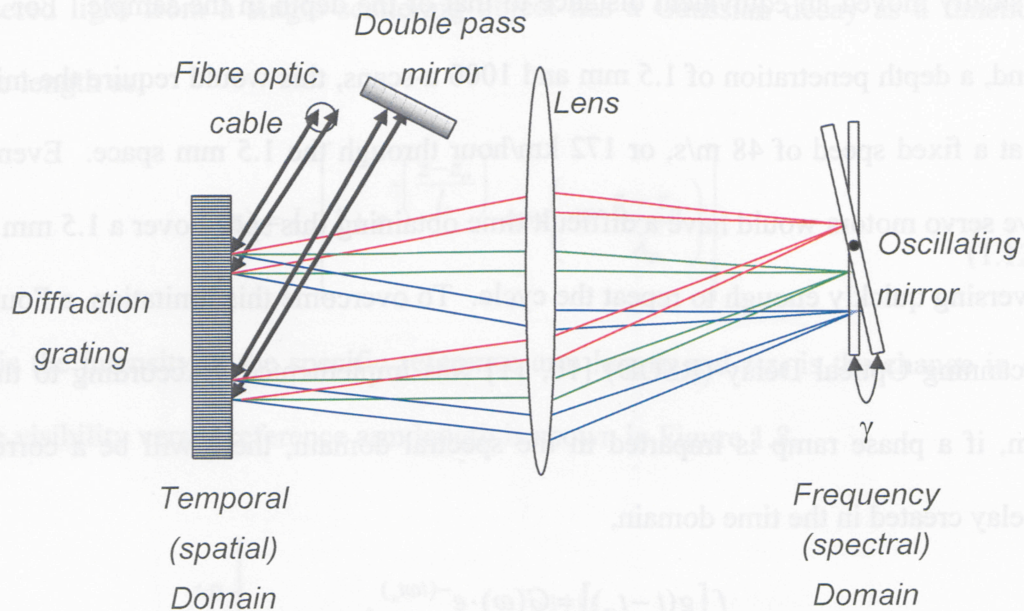


Figure 1.9 – Fourier domain Rapid Scanning Optical Delay Line (RSOD).

The laser light is separated into its frequency components and reflected through a convex lens towards an oscillating mirror, which oscillates on a fixed pivot point through a very small angle. This change in angle imparts a phase ramp to the incoming light components. The shifted spectral components are reflected through the lens and onto the grating to recombine before reflecting off of a double pass mirror. The double pass mirror returns the light back through the same path and into the fiber optic cable towards the interferometer. The returned light contains the time domain shift induced by the spectral phase ramp corresponding to a change in depth into the sample. The scanning rate of this system's RSOD is 8 kHz.

1.7 Signal Sampling and Processing

1.6.3 Fourier Domain Rapid Scanning Optical Delay Line (RSOD)

Since OCT runs on a digital system, sampling rates and signal processing methods play a large role in data processing.

1.7.1 Sampling Theorem and Aliasing

When an analogue signal is digitized, it is sampled a specific number of times over a given time interval. This is called the sampling frequency. In order to properly recreate the signal there is a minimum sampling frequency required. This minimum rate is called the Nyquist frequency and is defined as two times the highest frequency in the sample.

The reconstruction of an under sampled-signal will lead to aliasing. This means that an incorrect frequency becomes the alias of the correct one. Figure 1.10 shows an under sampled cosine wave. Note that the sampled data could represent either the original signal or a sine wave of significantly slower frequency.

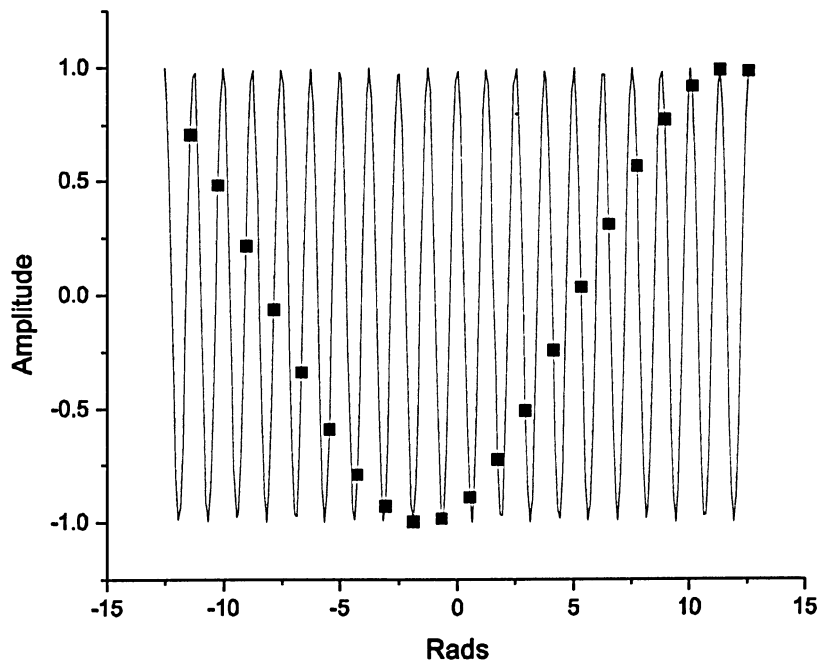


Figure 1.10 – Example of under sampling, the line is the signal while the dots represent the sampled data.

Another example of aliasing occurs with analogue clocks. As time passes, the arms on the clock move in a clockwise rotation. The small hand requires 720 minutes (12 hours) to complete one rotation while the large hand takes 60 minutes (1 hour). If one was to sample a clock every 12 hours + 1 minute, it would appear that the minute hand takes in fact 12 hours + 1 minute to move one notch. By this logic the hour hand would take ~30 days of this sampling rate to observe a change of one notch. This shows that sampling is too slow to determine the correct motion of the hands.

The autocorrelation method presented in the next chapter uses an arc tangent to determine phase information which has aliasing issues that are very similar to the previous example. This phase information is calculated using a four quadrant inverse tangent function which doubles the phase resolution over a two tangent arctangent. The range of the four quadrant function is $\pm\pi$ which gives a maximum change between two points of 2π rad.

Unwrapping methods [12] are used to detect a change between two adjacent points along one axis. When there is a change of 2π rad between adjacent points, the 2π rad complement is added to the remaining points. This requires a signal that has a good signal to noise ratio in order to perform unwrapping because noise spikes can also cause discontinuities in the data which can be mistaken for, or mask, 2π rad changes. However, even with the best unwrapping techniques available, the unwrapping is limited by the spectral resolution and the signal to noise ratio.

1.7.2 In-Phase and Quadrature Demodulation

Commonly referred to as I&Q demodulation, in-phase and quadrature demodulation are used quite extensively in signal processing and communications. By multiplying the incoming signal

by a reference signal and a reference signal shifted in phase by 90° , two orthogonal vectors are created. These two vectors are the real and imaginary frequency components of the incoming signal and are referred to as in-phase and quadrature components respectively. This can be seen in Figure 1.11

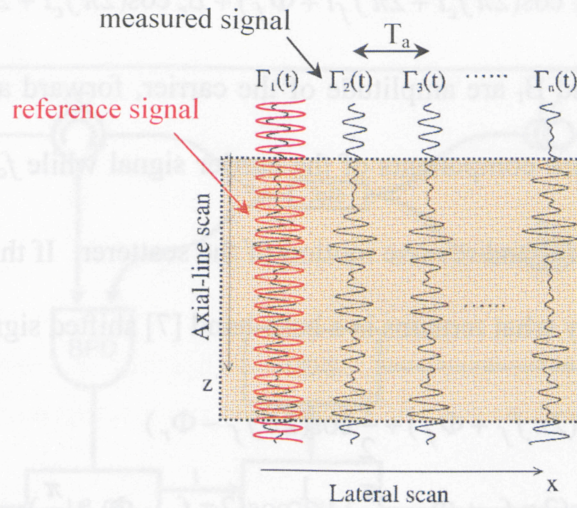


Figure 1.11 – Example of reference signal being compared to the measured signal. Courtesy of Victor Yang.

The deconstruction of the incoming signal into these components can be seen in Figure 1.12. By breaking a signal down into these vectors, one is able to easily obtain phase information.

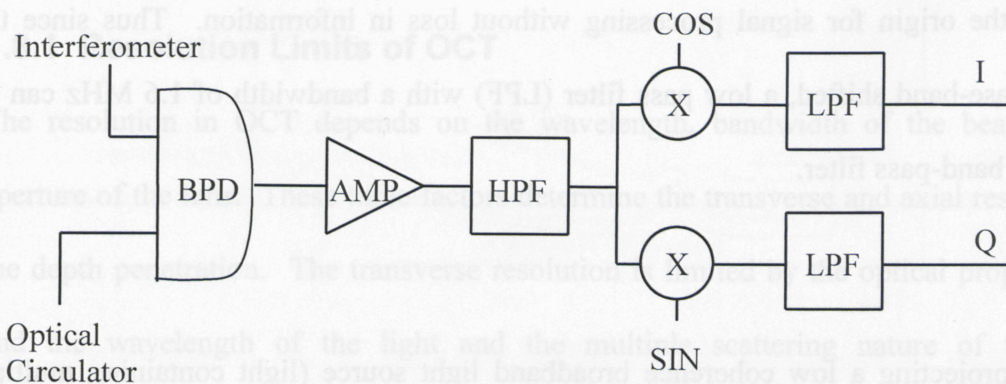


Figure 1.12 – Block Diagram of in-phase and quadrature demodulation. BPD Balanced Photo Detector; AMP Trans-impedance amplifier; HPF High Pass Filter; LPF Low pass filter.

In OCT signals, there are two frequency components. One of these is the carrier frequency while the other is the phase change introduced by the motion of the scattering object. This is represented [7] by,

$$\Gamma(t) = A \cos(2\pi f_c t + \Phi_c) + B_f \cos(2\pi f_c t + 2\pi f_f t + \Phi_f) + B_r \cos(2\pi f_c t + 2\pi f_r t + \Phi_r), \quad (1.14)$$

where Γ is the signal, A , B_f and B_r are amplitude of the carrier, forward and reverse signals, f_c and Φ_c are frequency and phase components of the carrier signal while f_c , f_c , Φ_f and Φ_r are components added by the forward and reverse motion of the scatterer. If this signal is multiplied by the original carrier frequency what remains is a base-band [7] shifted signal,

$$\begin{aligned} I(t) &= \frac{1}{2} B_f \cos(2\pi f_f + \Phi_f) + \frac{1}{2} \cos(2\pi f_f - \Phi_r) \\ Q(t) &= \frac{1}{2} B_f \cos(2\pi f_f + \Phi_f - \frac{\pi}{2}) + \frac{1}{2} \cos(2\pi f_f - \Phi_r + \frac{\pi}{2}) \end{aligned} \quad (1.15)$$

so it can be filtered out through use of a low pass filter. Phase estimation techniques can now make use of the orthogonal nature of the inphase and quadrature signal. The carrier frequency is 4.3 MHz with a bandwidth of 3.2 MHz. Since the signal is Gaussian in nature, it can be shifted in frequency to the origin for signal processing without loss in information. Thus since the signal is when base-band shifted, a low pass filter (LPF) with a bandwidth of 1.6 MHz can be used instead of a band-pass filter.

1.8 OCT

OCT works by projecting a low coherence broadband light source (light containing multiple frequencies in a Gaussian distribution) onto an object and processing the backscattered photons using interferometry to separate information based on depth. An optical coupler is used to

recycle the light that would normally be reflected back towards the light source. This is used for common-mode rejection at the balanced photo detector through subtraction of the DC bias. The interference pattern is captured by a balanced photo-detector, I&Q demodulated, filtered, digitized and then analyzed on a computer. A schematic diagram is shown in Figure 1.13.

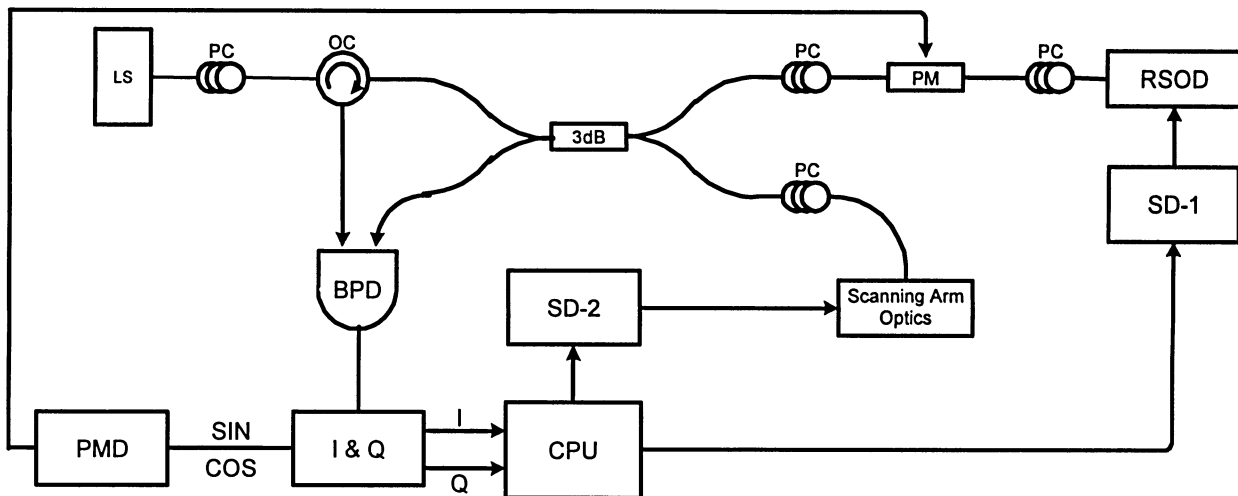


Figure 1.13 – LS: light source; PC: polarization controller; OC: optical circulator; 3 dB: 50-50 fiber coupler; PM: phase modulator; RSOD: rapid scanning optical delay line; BPD: balanced photo-detector; PMD: phase modulator driver; I&Q: inphase and quadrature demodulator; SD-1 & 2: scanner drivers; COMP: computer.

1.8.1 Resolution Limits of OCT

The resolution in OCT depends on the wavelength, bandwidth of the beam and numerical aperture of the lens. These three factors determine the transverse and axial resolution as well as the depth penetration. The transverse resolution is limited by the optical properties of the lens and the wavelength of the light and the multiple scattering nature of tissue. As with microscopes, resolution is limited to the numerical aperture of the beam which determines the

focal length and minimum spot size or size of the beam at its focal centre. The transverse resolution [9] is defined as,

$$\Delta x = \frac{4\lambda}{\pi} \left(\frac{f}{d} \right), \quad (1.16)$$

where Δx is the transverse resolution in metres, f is the focal length of the lens and d is its spot size. However, a large aperture means that there will be a small depth of focus, thus limiting the usable depth of imaging [9] to,

$$2z_R = \frac{\pi \Delta x^2}{2\lambda}, \quad (1.17)$$

where $2z_R$ is the usable depth. This relationship between aperture and resolution, versus depth tradeoff is illustrated in Figure 1.14.

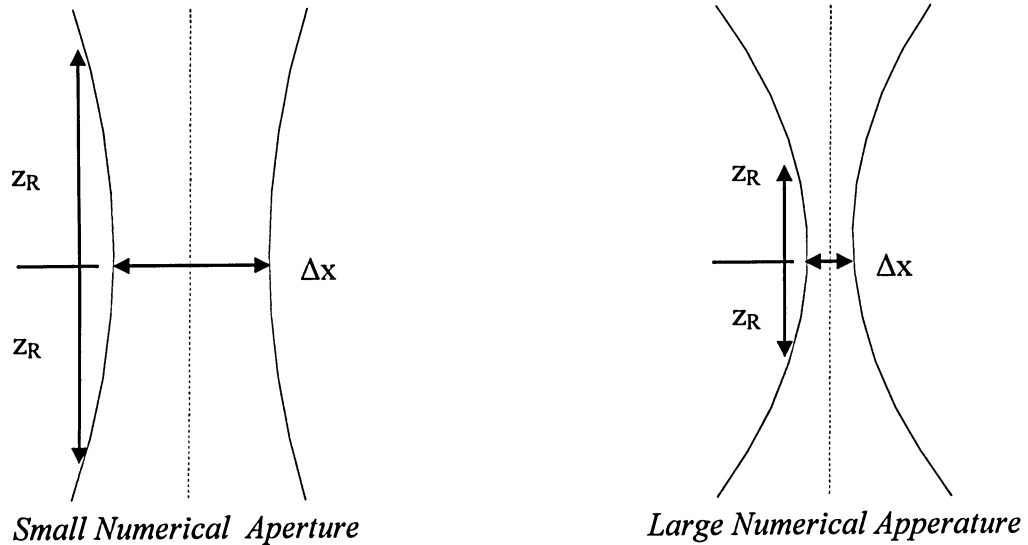


Figure 1.14 – Beam profiles for low and high numerical aperture showing relationship between depth and transverse resolution.

The axial resolution is determined by the coherence length in the interferometer. This relationship was stated earlier in equation (1.11). The resolution varies based on the square of the wavelength divided by the bandwidth. This relationship is plotted in Figure 1.15 .

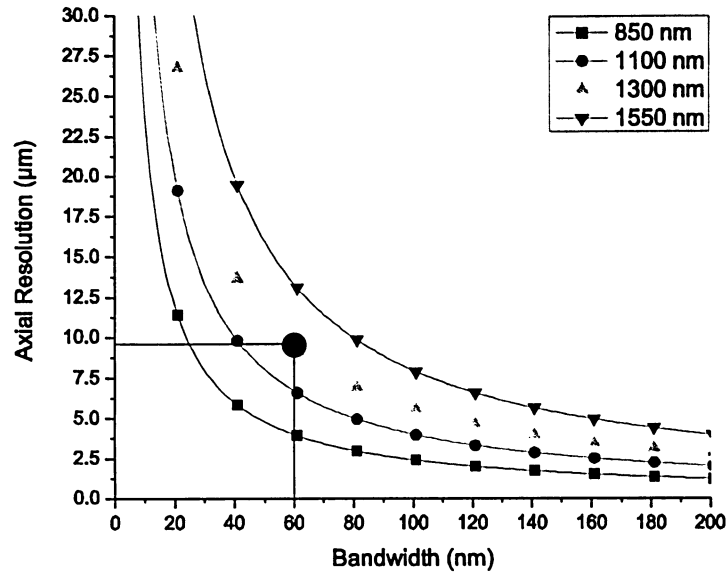


Figure 1.15 – Axial resolution versus bandwidth. Light with a 1.3 μm and 60 nm BW is highlighted.

The limiting parameters for imaging depth are absorption and scattering coefficients. Figure 1.16 shows the work of Sainter *et al* to determine the ideal optical wavelength.

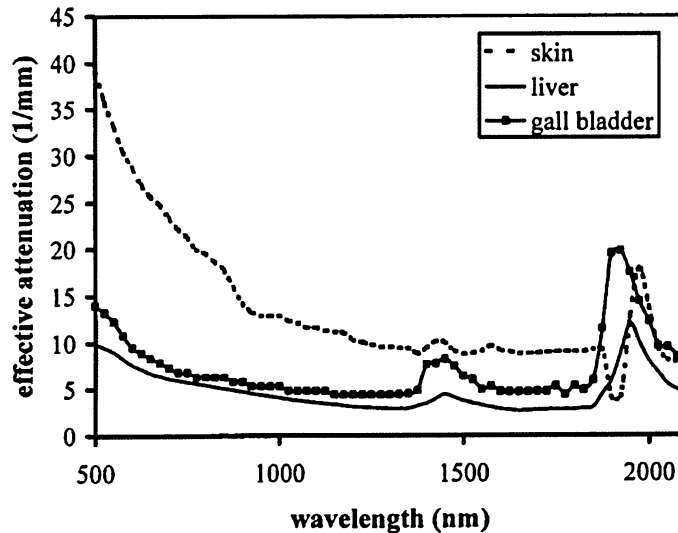


Figure 1.16 – Data courtesy of A.W. Sainter, T.A. King, M.R. Dickinson [13] represents the attenuation versus wavelength while The first peak depth penetration occurs at ~ 1400 nm.

As stated earlier, the resolution decreases as the wavelength increases. As the penetration depth increases with increased wavelength, there is a trade off between resolution and depth. As seen in Figure 1.16 the effective attenuation flattens out at $\sim 1400\text{nm}$. There are inexpensive commercially available broadband lasers available in the 1300 nm range, and this wavelength appears to offer a good tradeoff between resolution and depth penetration. This is the frequency of choice for most OCT systems that do not image the eye.

1.9 OCT versus Ultrasound

Throughout this literature comparisons are made between the signal processing algorithms in ultrasound and OCT. It is important to realize the similarities between these two modalities in terms of signal processing. Both these modalities undergo in-phase and quadrature demodulation of the incoming signal. The carrier signal of the ultrasound is between 2-20 MHz while in this OCT system it is 4.3 MHz. The axial scanning frequency of the OCT system is analogous to the pulse repetition frequency in ultrasound and both modalities have the option of digitizing the captured data at a rate acceptable for their hardware setup which is on the order of MHz.

For velocity estimation, OCT has a much smaller voxel size than ultrasound. The velocity estimate derived for either of these two modalities is the mean velocity in the given volume. However, the resolution OCT is roughly $10\text{ }\mu\text{m} \times 10\text{ }\mu\text{m}$ whereas clinical 3 MHz clinical ultrasound would have a resolution of $1.1\text{ mm} \times 2.8\text{ mm}$. Because a red blood cell is $\sim 7\text{ }\mu\text{m}$, the estimate of velocity on an OCT system with a $10\text{ }\mu\text{m}$ resolution at any given point can be to be the actual velocity of the scattering object.

2 Chapter 2: Methods

There are several techniques for estimation of motion using the backscattered data on OCT systems. The captured data on this OCT machine was already setup for hardware I&Q demodulated for use with the Kasai [2, 10, 14-17] autocorrelation estimator. The Kasai method is a phase based velocity estimation technique applied in the transverse direction. A variant on the Kasai method was suggested by Loupas *et al* [18, 19] for Doppler ultrasound which makes use of a two-dimensional (2D) autocorrelation function. This is called the 2D Kasai and it takes advantage of information in both the axial and the transverse direction. Other phase based methods, such as the short time fast Fourier transform (STFFT), have been reported [20-22] but are computationally more complex.

The method proposed for this thesis was a Kasai based estimator using both transverse and axial data and is performed without hardware changes to current generation OCT systems utilizing I&Q demodulated for Kasai estimation [14, 15, 17, 23, 24].

2.1 Phase Based Velocity Estimation Techniques

Signals that are captured by this system are compared to a reference wave and separated into inphase and quadrature components which are represented by,

$$\Gamma(t) = \mathbf{I}(t) + j\mathbf{Q}(t), \quad (2.1)$$

where Γ is the signal and \mathbf{I} and \mathbf{Q} . Using these two vectors, the phase can be calculated using a four-quadrant arctangent function where,

$$\phi(t) = \arctan\left(\frac{Q(t)}{I(t)}\right), \quad (2.2)$$

which determines the phase at any given point with a range of $-\pi$ to π . To determine the phase shift over a given time interval, the derivative of the phase is taken with respect to time. Since data is digitally captured, a discrete approximation of the derivative [7] is used,

$$\frac{d\phi(t)}{dt} \approx \frac{\Delta\phi(i)}{\Delta i} = \frac{Q(i)I(i-1) - I(i)Q(i-1)}{Q^2(i) + I^2(i)}, \quad (2.3)$$

where i is the index number of the digital sample. This gives the digital approximation for the phase change estimation between two adjacent points in time. This phase estimation can be converted to frequency through,

$$\Delta f = \frac{1}{2\pi T_s} \Delta\Phi, \quad (2.4)$$

where Δf is the change in frequency, T_s is the time between two samples and $\Delta\Phi$ is the change in phase over time.

2.2 Kasai Autocorrelation Estimation

The original estimator proposed by Kasai [2], was based on the phase estimation technique mentioned in section 2.1. This was a breakthrough for color flow imaging with ultrasound since it provided real-time flow measurements. To increase the reliability of the phase estimation, the in-phase and quadrature signals were averaged across an axial length of M samples before calculating phase change, effectively collapsing the line scan to a single depth point. The collapsed data point is then averaged across a transverse length of N scan lines to increase the signal to noise ratio (SNR). As this estimator collapses the points before phase estimation, it is

called the 1D Kasai. This formula, when applied to demodulated OCT data, can be used to estimate the change in frequency [2] by,

$$f_{1D} = \frac{f_a}{2\pi} \arctan \left(\frac{\sum_{n=0}^{N-2} \left[\left(\sum_{m=0}^{M-1} Q(m, n) \right) \left(\sum_{m=0}^{M-1} I(m, n+1) \right) - \left(\sum_{m=0}^{M-1} I(m, n) \right) \left(\sum_{m=0}^{M-1} Q(m, n+1) \right) \right]}{\sum_{n=0}^{N-2} \left[\left(\sum_{m=0}^{M-1} I(m, n) \right) \left(\sum_{m=0}^{M-1} I(m, n+1) \right) + \left(\sum_{m=0}^{M-1} Q(m, n) \right) \left(\sum_{m=0}^{M-1} Q(m, n+1) \right) \right]} \right), (2.5)$$

where f_a is the axial scanning frequency and m and n are the axial and transverse indices of the inphase and quadrature signals. The original Kasai method performed phase estimate in the transverse direction and is referred to as the one-dimensional (1D) Kasai. This estimate assumes that there is a constant centre frequency across all data points. Again, since this is a phase based estimation, the frequency change predicted by this method can be used directly in equation (2.4) to predict the velocity.

Loupas *et al* proposed a way to compensate for the shift in the backscattered frequency. In I & Q demodulation, a change in the backscattered frequency would no longer match the frequency of the reference signal and thus the demodulation would be affected. By applying an autocorrelation in the depth direction, the mean backscattered carrier frequency at each point can be estimated and used to correct the estimate in the transverse direction. The following proof was the one provided by Loupas [18], demonstrating that the axial autocorrelation does estimate the mean backscattered carrier frequency. Assuming an array $\hat{r}(m, n)$, of size $M \times N$ its autocorrelation $\hat{\gamma}(m', n')$ is given by,

$$\hat{\gamma}(m', n') = \sum_{m=0}^{M-m'-1} \sum_{n=0}^{N-n'-1} \hat{r}(m, n) \hat{r}^*(m+m', n+n'). \quad (2.6)$$

The 2D Fourier transform, $\hat{\Gamma}$, is the inverse Fourier transform of the 2D autocorrelation function,

$$\hat{\gamma}(m', n') = \sum_{m=-M/2}^{M/2-1} \sum_{n=-N/2}^{N/2-1} \hat{\Gamma}\left(\frac{m}{M}, \frac{n}{N}\right) e^{j\left(\frac{2\pi m m'}{M}\right)} e^{j\left(\frac{2\pi n n'}{N}\right)}. \quad (2.7)$$

In order to prove that the autocorrelation in the depth direction is equal to the mean backscattered carrier frequency, equation (2.7) is differentiated at $m' = n' = 0$ to get

$$\left. \frac{\partial \hat{\gamma}(m', n')}{\partial m'} \right|_{m'=n'=0} = \sum_{m=-M/2}^{M/2-1} \sum_{n=-N/2}^{N/2-1} j \frac{2\pi m}{M} \hat{\Gamma}\left(\frac{m}{M}, \frac{n}{N}\right), \quad (2.8)$$

Since m/M and n/N correspond to the discrete normalized frequencies f and F , respectively, the equation (2.8) can be simplified to,

$$\langle f \rangle = \frac{\frac{-j}{2\pi} \left. \frac{\partial \hat{\gamma}(m', n')}{\partial m} \right|_{m'=n'=0}}{\hat{\gamma}(0, 0)}. \quad (2.9)$$

Assuming that the real part is an even function and the imaginary is odd, this simplifies to,

$$\langle f \rangle = \frac{1}{2\pi} \left. \frac{\partial \theta(m', n')}{\partial m'} \right|_{m'=n'=0}, \quad (2.10)$$

which for the smallest $m=1$ can be approximated by

$$\langle f \rangle = \frac{1}{2\pi} \frac{\theta(m', 0) - \theta(0, 0)}{m'}, \quad (2.11)$$

This shows that the mean frequency can be estimated by an autocorrelation in the depth direction. Applying this to the 1D Kasai and estimating each phase shift before averaging rather than collapsing the data into a single point before calculating, Loupas proposed the two-

dimensional (2D) Kasai estimator using a two-dimensional autocorrelation. The combined phase estimate, for Doppler ultrasound systems, with backscattered frequency correction [19] is,

$$v_{2D} = \frac{c}{2} \frac{\frac{1}{2\pi T_s} \arctan \left(\frac{\sum_{m=0}^{M-1} \sum_{n=0}^{N-2} [Q(m,n)I(m,n+1) - I(m,n)Q(m,n+1)]}{\sum_{m=0}^{M-1} \sum_{n=0}^{N-2} [I(m,n)I(m,n+1) + Q(m,n)Q(m,n+1)]} \right)}{\frac{1}{2\pi t_s} \left[2\pi f_{dem} + \arctan \left(\frac{\sum_{m=0}^{M-2} \sum_{n=0}^{N-1} [Q(m,n)I(m+1,n) - I(m,n)Q(m+1,n)]}{\sum_{m=0}^{M-2} \sum_{n=0}^{N-1} [I(m,n)I(m+1,n) + Q(m,n)Q(m+1,n)]} \right) \right]}, \quad (2.12)$$

where f_{dem} is the normalized counterpart of the reference sinusoid, t_s is the axial sampling interval, T_s is the pulse repetition period and c is the speed of the sound wave in the medium.

2.3 Transverse Kasai Autocorrelation Estimate

The TK algorithm is a modified transverse method, proposed by Loupas in the previous section and it calculates phase change and then averages rather than collapsing the points before calculation. Therefore the TK estimation is less noisy than the 1D Kasai, and does not require any additional calculations. The TK is defined as,

$$f_{TK} = \frac{f_a}{2\pi} \tan^{-1} \left\{ \frac{\sum_{m=0}^{M-1} \sum_{n=0}^{N-2} [Q(m,n)I(m,n+1) - I(m,n)Q(m,n+1)]}{\sum_{m=0}^{M-1} \sum_{n=0}^{N-2} [I(m,n)I(m,n+1) + Q(m,n)Q(m,n+1)]} \right\}, \quad (2.13)$$

which is able to accurately estimate the Doppler frequency with a resolution of $\pm f_a/2$, or ± 4 kHz on this system. After 4 kHz, aliasing rings occur. These can be unwrapped to an extent determined by the signal to noise ratio of the acquired signal. When the SNR is high and the rings are well defined and separated, one is able to unwrap the rings caused by aliasing. The

velocity resolution on the TK has been shown to be as low as $2 \mu\text{m/s}$ [10] at a 81° angle. Since the TK estimates the change in phase between two adjacent a-scans, f_{TK} does not require a background carrier subtraction in order to estimate the Doppler frequency.

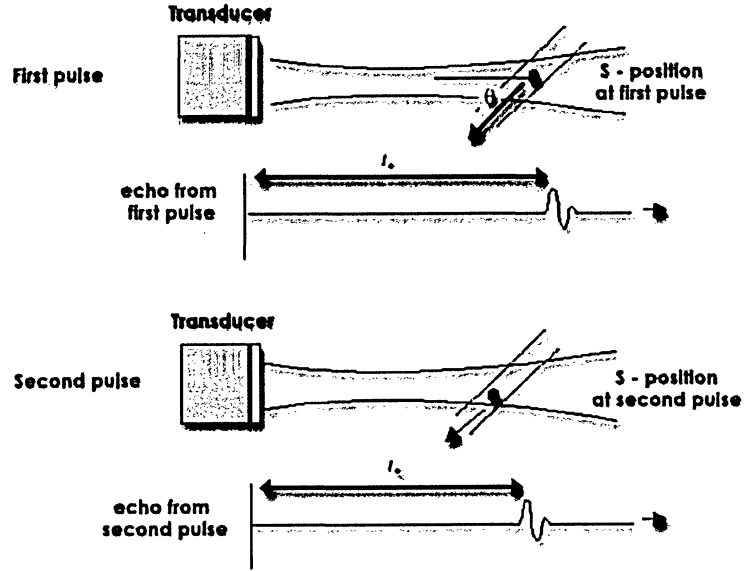


Figure 2.1 – Example of TK estimation between two pulses [25].

As suggested by equation (2.11), the mean frequency can be estimated by an autocorrelation in the axial direction of demodulated I&Q data.

2.4 Proposed Algorithm: The Axial Kasai

In a literature search, previous work was found that detected a change in the backscattered carrier frequency as attributed to the motion of the scattering object as large as 300 Hz in the using the short time fast Fourier transform (STFFT) [26]. The detection of the Doppler shift through this mechanism suffers from high computational complexity and requires a large amount of axial data in order to obtain an accurate estimate. In order to obtain sufficient data points for the STFFT to accurately measure the shift, a capture time of 16 seconds was required per frame [27].

Since the autocorrelation in the axial direction has been shown to estimate the mean backscattered carrier frequency by Loupas, it was believed that a modification of their 2D Kasai estimation could be used to detect the effect of the Doppler shift on the backscattered signal. This method is what has been proposed as the main portion of this MASc research project. The literature search revealed two previous attempts at performing mean carrier frequency estimation through use of axial data, both of which were hardware implementations. One implementation was by Izatt *et al* [28], the other by Bopart *et al* [29]. However both of these methods lacked either low end velocity detection or did not have good resolution.

In addition to the proposed axial estimation, it is proposed that a combination of the TK coupled with the proposed modification to the Kasai, which we call the axial Kasai (AK), will allow for estimation of a wide range of frequencies. This is a novel estimation technique because it utilizes frequency estimation through two spatial dimensions and can be implemented in OCT systems in software as opposed to complex hardware implementations. The proposed AK variation in Kasai estimation to detect the mean backscattered carrier frequency is,

$$f_{AK} = \frac{f_s}{2\pi} \tan^{-1} \left\{ \frac{\sum_{m=0}^{M-2} \sum_{n=0}^{N-1} [Q(m,n)I(m+1,n) - I(m,n)Q(m+1,n)]}{\sum_{m=0}^{M-2} \sum_{n=0}^{N-1} [I(m,n)I(m+1,n) + Q(m,n)Q(m+1,n)]} \right\}, \quad (2.14)$$

where f_s is the sampling frequency in the axial direction. The theoretical frequency limits on the frequency detection of this method are $\pm f_s/2$, where f_s is in the MHz range. Since the AK is an estimation of the mean backscattered carrier frequency, to obtain the Doppler shift AK

results from a stationary background source need to be subtracted from the AK of a moving source. Thus, the doppler frequency is,

$$f_D = f_{AKmoving} - f_{AKstationary}, \quad (2.15)$$

where $f_{AKmoving}$ is the AK result for the moving scatterer and $f_{AKstationary}$ is the AK result for the stationary AK estimate.

3 Chapter 3: Experiments and Results

To determine whether the proposed algorithm in Chapter 3 could work, first a controlled flow phantom experiment then *in vivo* experiment was performed. Images were acquired using a time-domain DOCT system containing a 5 mW broadband light source centered at 1.3 μm with 63 nm bandwidth. The axial scanning rate was $f_a = 8$ kHz, using a rapid-scanning optical delay (RSOD) line in the reference arm. A phase modulator, as seen in Figure 1.13, produces a carrier frequency of 4.3 MHz. The hardware demodulated I&Q signals were processed using the TK and AK for window sizes ranging from $N = 2$ to 32 and $M = 16$ to 32.

There were two experimental variations. First, a flow phantom experiment was setup to investigate steady state flow through a glass capillary using Intralipid as a scatterer. Flow was controlled using both a constant gravity fed system and then later using a medical infusion pump capable of a large range of flow rate selections. In the third experiment, *in vivo* endoscopic DOCT data from a rat esophagus was collected.

3.1 Experiment 1 – Gravity Fed Flow Phantom

In this experiment, a gravity fed flow system was used to obtain accurate flow rates. The gravity ‘pump’ consisted of three sections: Main cylinder, overflow cylinder and fluid reservoir. To obtain accurate volumetric data, large time intervals ranging from 5 to 40 minutes were used. The slower flow rates required a longer duration in order to collect enough liquid. This method is the most accurate, but takes >5 hours.

The main cylinder was at the top of the experiment and held ~2 liters of fluid. Gravity acted upon the fluid in the open topped main cylinder. This pressure drove the liquid through the connecting tubes and into the glass capillary used for the experiment. There were two holes in the bottom of the main cylinder; the first received fluid from a return pump while the second was connected to the experimental apparatus. Since the return pump was continuously operating, the only path available for the fluid to flow was through the experiment or to overflow over the top of the cylinder.

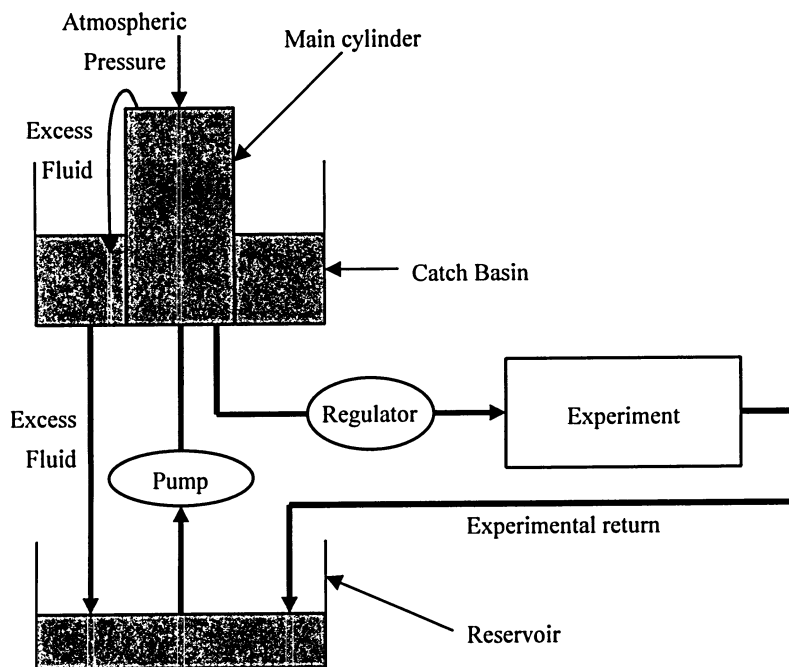


Figure 3.1 – Diagram of the gravity flow setup.

The main cylinder fed liquid to the experiment and thus loses volume over time. The reduction in volume would create a corresponding loss in pressure and flow rates. To avoid this, a return pump was used to keep a continuous flow of fluid moving between the main cylinder and the reservoir. As the liquid was pumped from the reservoir into the cylinder at a high rate of flow,

the main cylinder overflowed and excess liquid was returned to the reservoir creating a closed system. If the incoming flow rate from the pump was larger than the flow rate channeled to the experiment, the volume of the main cylinder and the corresponding pressure remain constant. The pump had a maximum flow rate of 10 L/hour while the maximum flow rate in the experiment was 0.2 L/hour ensuring a constant rate of flow. A picture of the experimental setup is shown in Figure 3.2.

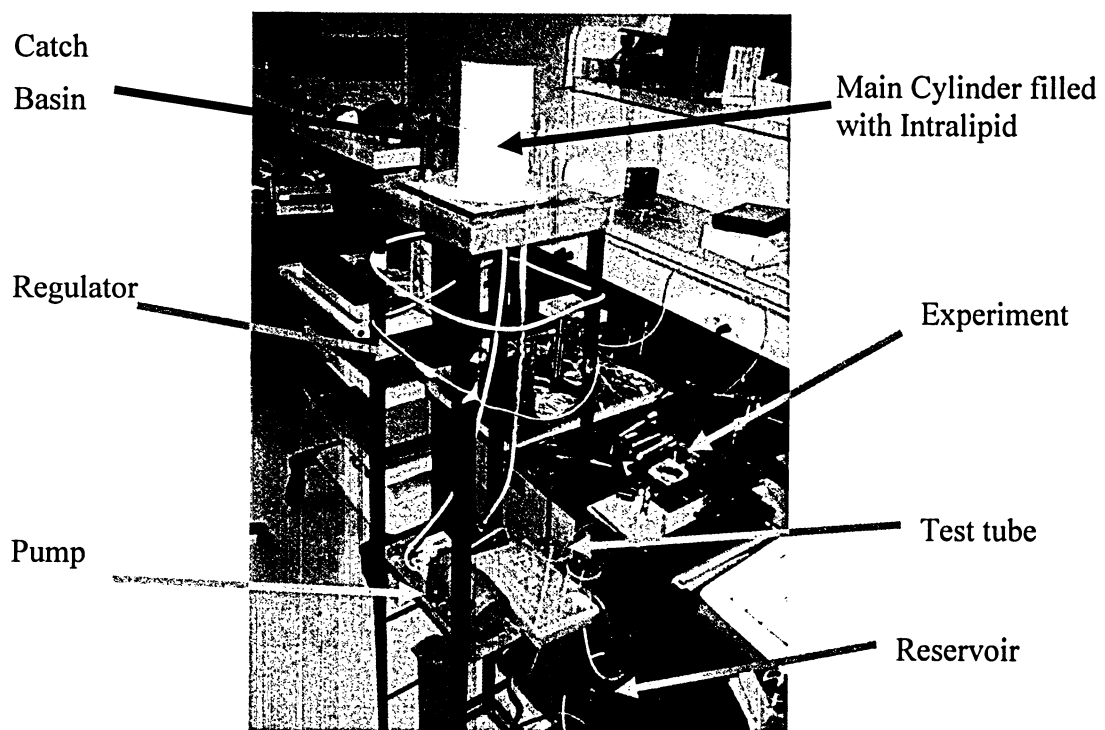


Figure 3.2 – Picture of experimental gravity pump setup.

3.1.1 Angle

One of the factors involved in the accurate determination of the Doppler frequency is the angle at which the laser is incident on the medium under motion. A compass was used to level the incident angle of the beam and then used to measure the angle. The setup shown in Figure 3.3

was used to measure the angle with a error of $\pm 1^\circ$. The set angle for the first batch of experiments was 86° . The index of refraction also caused the light to bend, and was factored in using equation (1.9).

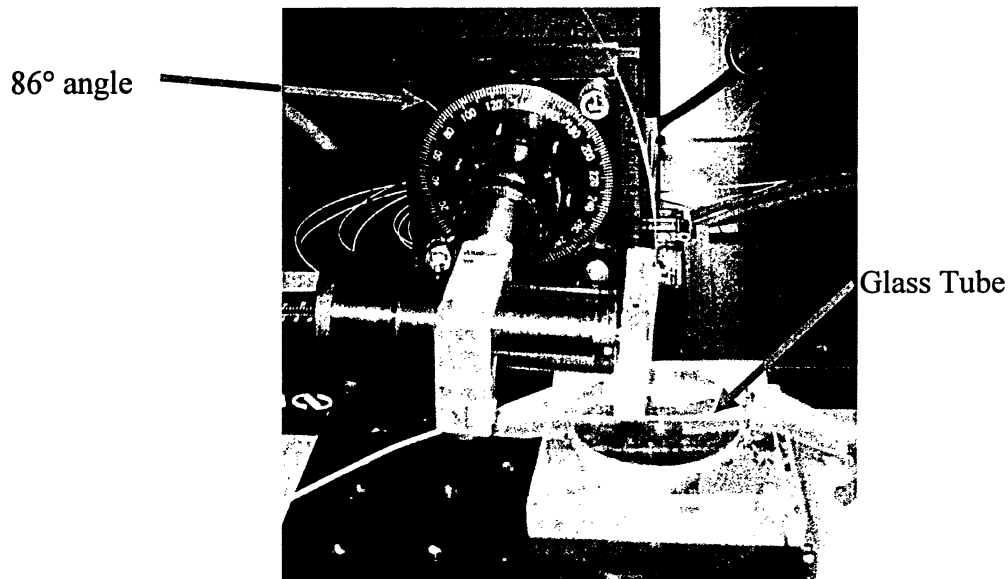


Figure 3.3 – Experimental Apparatus with a Doppler angle of 86° .

3.1.2 Experimental Flow measurement

To determine the flow rate of the experiment, the return was diverted from the reservoir to a test tube. The mass of the test tubes were measured to ± 0.1 mg before use. The time it took to fill $\sim 1/3$ of the test tube was recorded and then the mass was measured. Time intervals varied from 5 minutes to 40 minutes for each test tube. Factoring in human reaction time the uncertainty of start and stop times would be within ± 3 seconds resulting in a maximum deviation of 1% for a 5 minute trial or 0.04% deviation for a 40 minute trial. The mass of the tube with solution was ~ 30 g, so there is a small component of error from the measurement of mass. The mass after experimentation was subtracted from the pre-experimentation mass to determine how many grams of liquid were collected over the measured interval. Assuming that the mass of the

solution is roughly equal to that of water, the volume per unit time was calculated. These flow rates were then processed with equation (1.3) to determine the centre velocity.

Volume of Solution	2.5 L
Solution Contents	1% Intralipid, 99% distilled water
Density of solution	0.9955 kg/L
Viscosity	1.36 cP
Inner Radius of Tube	0.5 mm
Outer Radius of Tube	0.7 mm
Length of Tube	5 cm
Cross sectional area	196 μm^2
Angle	86°
Re Range	<1 to 300
Entrance Length Range	<0.1 mm to 5 mm

Table 3.1 – Experimental Parameters.

3.1.3 Low-Flow Experimental Observations

To visually demonstrate the prediction capabilities of the TK phase based estimation algorithms, as well as unwrapped versions, four select velocity profiles were plotted in Figure 3.4. The predicted parabolic curve was determined using the flow rate measured in section 3.1.2 and equation (1.2). Since the Doppler angle is very close to being perpendicular, the aliasing limits are ± 21 mm/s. The first profile shows low velocity data with a maximum speed of 800 $\mu\text{m/s}$ which generates a peak Doppler frequency of ~ 120 Hz. When the peak velocity is increased to ~ 17 mm/s, a Doppler frequency of ~ 2.5 kHz was generated. This is roughly in the centre of the 4 kHz detection range of the TK and is shown in B. The first occurrence of aliasing occurs, at expected at a velocity of 21 mm/s and is unwrapped in C. Note that the unwrapper when

averaged over 8000 lines performs a good estimate when compared to predicted values. An unwrapping program can be used to unwrap multiple aliasing rings as shown in D.

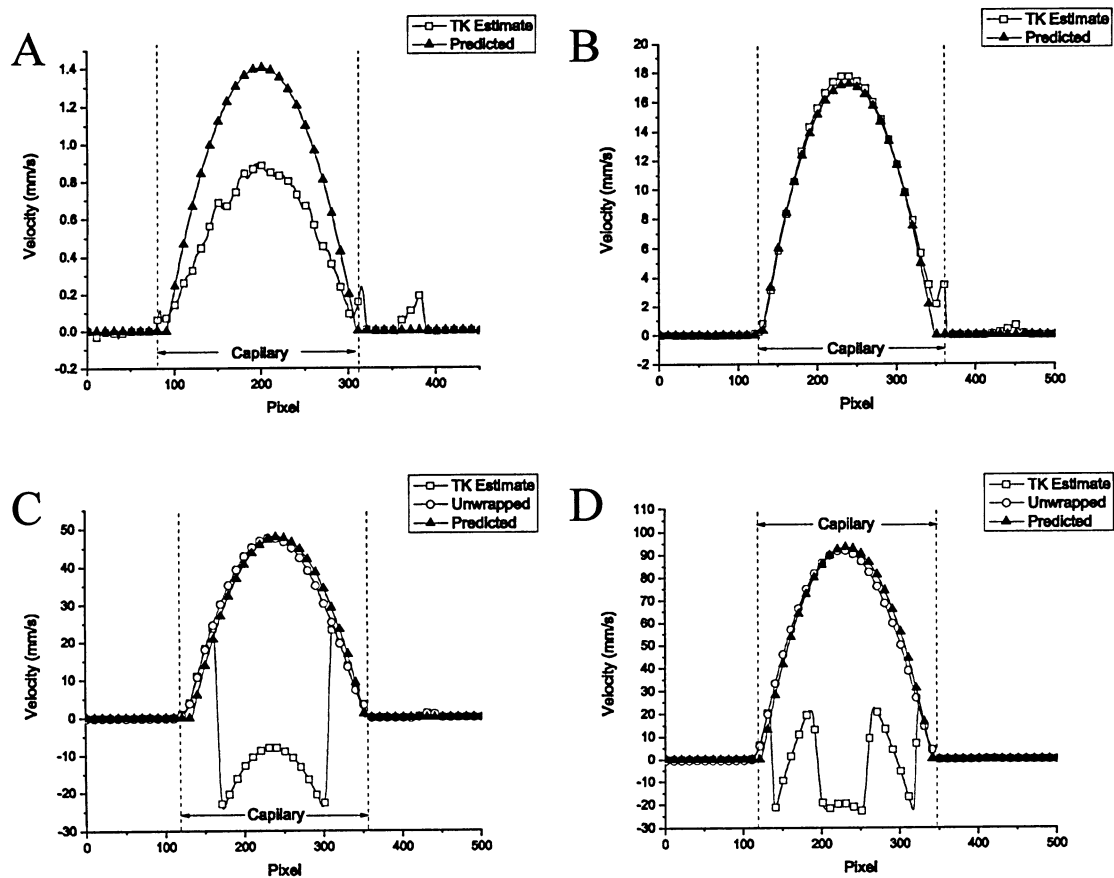


Figure 3.4 – Select flow profiles demonstrating accuracy of TK estimate. A) slow flow B) flow at half velocity detection at this angle C) Flow causing 1 aliasing ring D) flow causing 2 aliasing rings.

Due to the near vertical angle of incidence, a change in the result from the AK *was not visible at these speeds*. For all flow rates, the AK result appeared to be the same within experimental error. However, when the angle was decreased a change was noticed in the AK signal processing which was the basis for experiment 2.

3.2 Experiment 2 – Wide Range of Flow

A second flow phantom experiment was performed to further investigate the AK at a larger Doppler angle with wide range of flow rates. This experiment was performed using a calibrated medical infusion pump with a flow rate control function. The infusion pump, shown in Figure 3.5A is accurate to within 0.05 ml/hour and was able to apply a rate of 200 ml/hour through the 0.5mm ID capillary and 160 data sets were obtained. This experiment used a higher incident angle. To measure this angle, a digital photograph was taken of the setup as see in Figure 3.5B which was measured to be $\sim 44^\circ$. To ensure accurate calculation of the angle, this result was compared to the size of the tube as imaged by the OCT system. The inner diameter of the tube was measured to be 0.5 mm by the manufacturer. The depth, as it appears on the structural image appeared larger due to the Doppler angle, and is consistent with an angle of 44° .

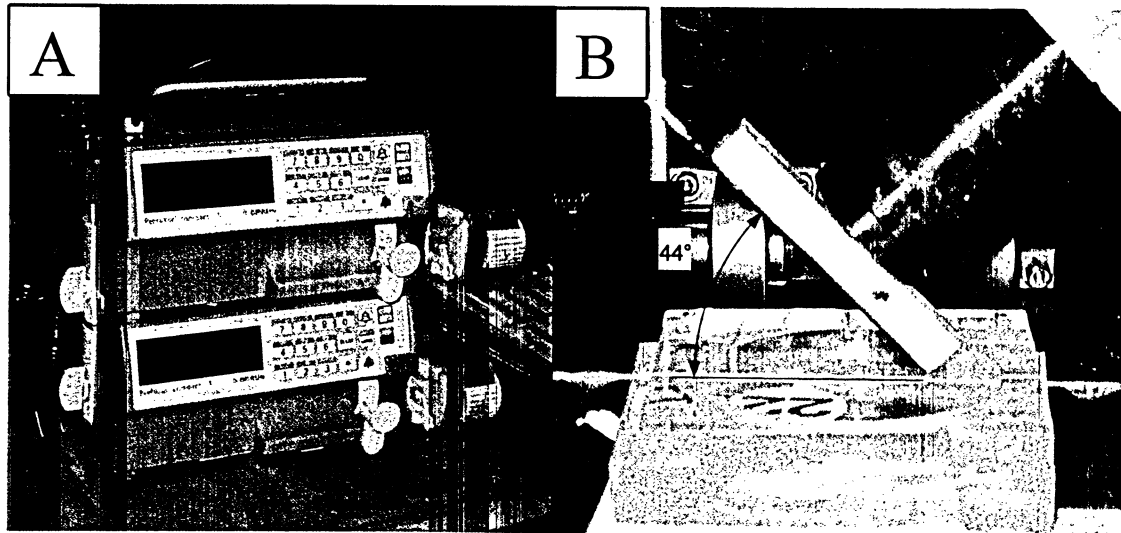


Figure 3.5 – Digital picture of experimental setup A) medical infusion pump B) picture of probe mounted to a scanning reference arm, probe can be seen on the bottom of the reference arm.

The infusion pump had a maximum flow rate of 200 mL/hour or a maximum peak centre velocity of ~ 57 cm/s. To drive the flow faster, a 50 mL syringe was epoxied to the connecting

line of the experiment. When a weight of ~200 pounds was applied, a peak velocity through the tube of > 2 m/s was obtained. At a velocity of ~2 m/s the entrance length was calculated using equation (1.4) to be 13.4 mm and Reynolds number was calculated from equation (1.1) to be 730; laminar parabolic flow was therefore assumed for all flow rates. The tube was imaged using a stationary probe to acquire data along one location as a function of time for M-mode imaging.

Flow phantoms with flow speeds ranging from 130 $\mu\text{m/s}$ to 57 cm/s were analyzed using the AK equation (2.14) with $N=32$ and $M=32$ and averaged over 1000 a-scans to increase SNR. Select AK frequency results are shown in Figure 3.6A for bidirectional flow. As the estimate was the mean backscattered carrier frequency, bidirectional velocities were obtained by subtraction of the stationary signal. When this frequency data was used as the Doppler shift, Figure 3.6B was generated. This figure is a family of parabolic profiles in good quantitative agreement with the experimentally set flow rates and calculated peak velocities assuming a laminar profile.

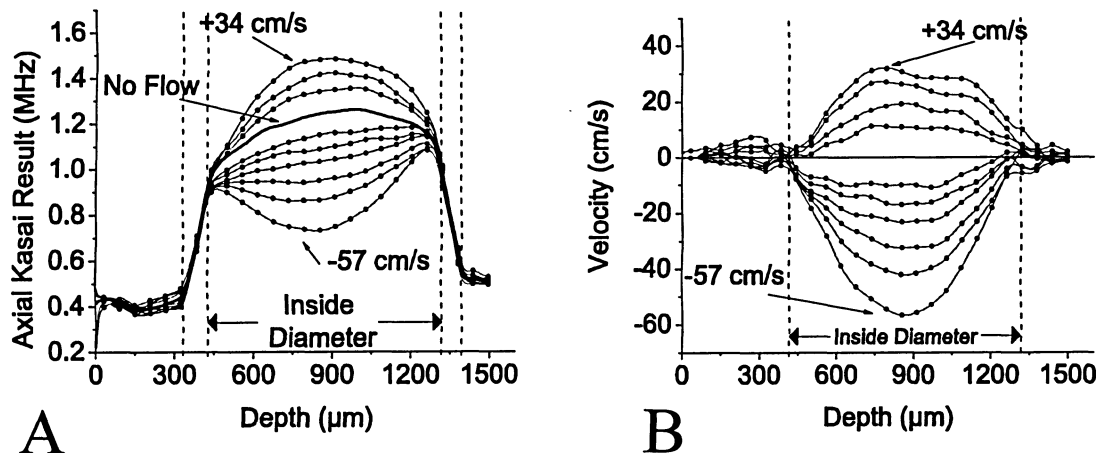


Figure 3.6 – (A) Change in the AK estimated frequency as a function of flow velocity. When no-flow AK (solid line) result subtracted from the flowing channels, a family of parabolic shapes is obtained (B);

Positively labeled velocities indicate flow towards the detector, negative velocities are away. Peak flow velocities are +34, +20, +11, no flow, -11, -19, -25, -34, -43 and -57 cm/s from top to bottom.

The estimated centre velocity from the AK and TK was then separated from the profile and plotted in Figure 3.7A; note the close linear relationship between the AK & TK predicted velocities versus the experimentally controlled velocities through the range of -57 cm/s to 34 cm/s. Note that flow rates estimated with flow heading towards the receiver falls off above 34 cm/s which correspond to a Doppler shift of ~ 0.400 MHz. This is due to the Doppler shift increasing the carrier frequency from 4.3 MHz to close to the Nyquist frequency of 5 MHz due to the 10 MHz sampling rate causing a filtering of the signal. Figure 3.7B demonstrates that there are three distinct flow regimes in the Kasai detection space. Zone I and II can be detected by the TK, and by TK with phase unwrapping, but not with the AK. At the transition region between zone II and III, the phase-unwrapped TK begins to severely underestimate the true velocities. However, the AK is still able to accurately measure velocities throughout zone III.

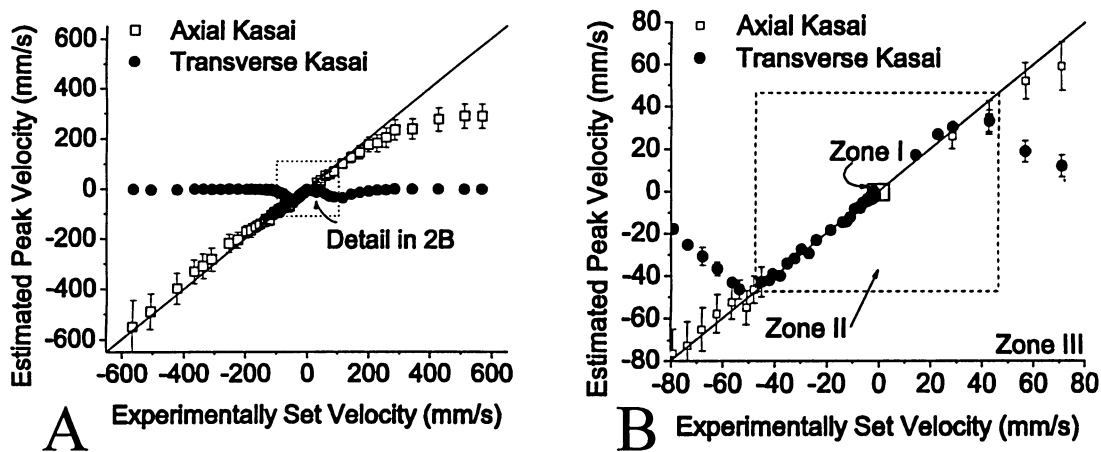


Figure 3.7 - TK and AK estimated peak velocities are compared to experimental peak velocities. (A) Peak velocities derived from TK and AK algorithms recorded over a large range of velocities. (B) A detailed view of TK shifts for lower flows. Error bars are result of standard error. The solid line is the line of identity.

Since flow rates above 57 cm/s were not feasible using the infusion pump they were not included on Figure 3.7. In order to determine the maximum away flow, a manually set high-flow rates of >2 m/s was processed using the AK. The results are shown in Figure 3.8. The exact flow rate is unknown, but the Axial Kasai predicts a change in frequency up to 1800 kHz before the backscattered signal is no longer apparent. This is in good agreement with Doppler shift pulling the returned carrier frequency out of the ± 1.6 MHz bandwidth of the system.

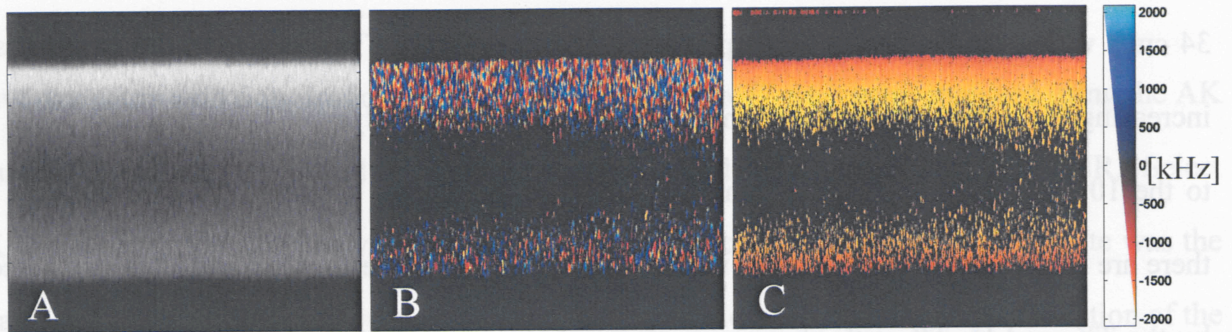


Figure 3.8 – Ultrafast M-Mode flow image. A) Structural image range 6dB to 72dB. B) TK range -4 kHz to 4kHz. C) AK range 2 MHz to 2 MHz. When the Doppler shift increases to 1800 kHz that the signal begins to vanish in all three images as predicted.

Appropriate values for N and M were determined based on an analysis of error versus gate size.

For the experimental analysis, an error rate of less than 5% was considered acceptable.

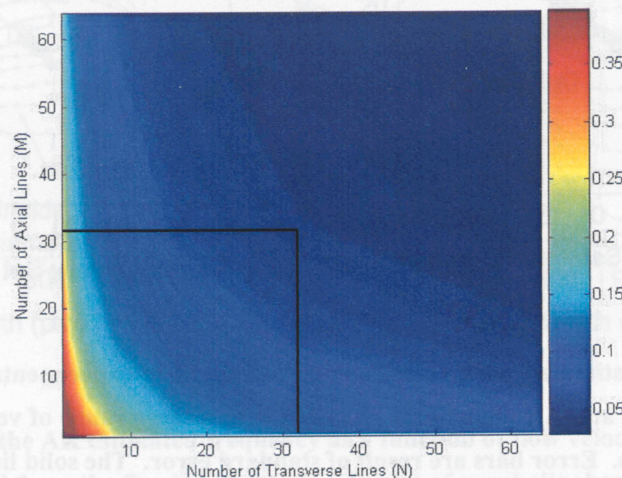


Figure 3.9 – Contour map of error versus a change in N and M. N=M=32 is highlighted.

To explore the relationship between N , M and error the standard deviation and mean values were calculated on the previous data. Figure 3.9 was generated using the results from 8000 a-scans. It can be seen from Figure 3.9 that the minimum number of points to average is $N=M=32$ or an area of 1024 points.

Figure 3.10 shows structural, TK and AK M-mode images generated with steady state peak velocities of 1.2 mm/s, 42 mm/s, and 155 mm/s using a window size of $N = 32$ and $M = 32$. These three velocities occur in zones I, II and III respectively. In zone I, the TK shows a parabolic profile with the pulsing effect inherent with use of the pump; in zone II, defined aliasing rings are evident and can be phase unwrapped. In zone III, the aliasing rings occurring with the TK are smaller than the axial resolution, so phase unwrapping cannot be reliably performed. For the AK analysis, a variance threshold algorithm was applied to the AK results, effectively negating its utility in the low flow regions of zones I and II, but permitting accurate and un-aliased flow estimation in zone III. The variance of the TK was calculated [9], which is a measure of the amount velocity spread over the given estimate window. It has been documented that this is an possible way to detect higher flow rates than the TK [9], but in this case was used to threshold the AK.

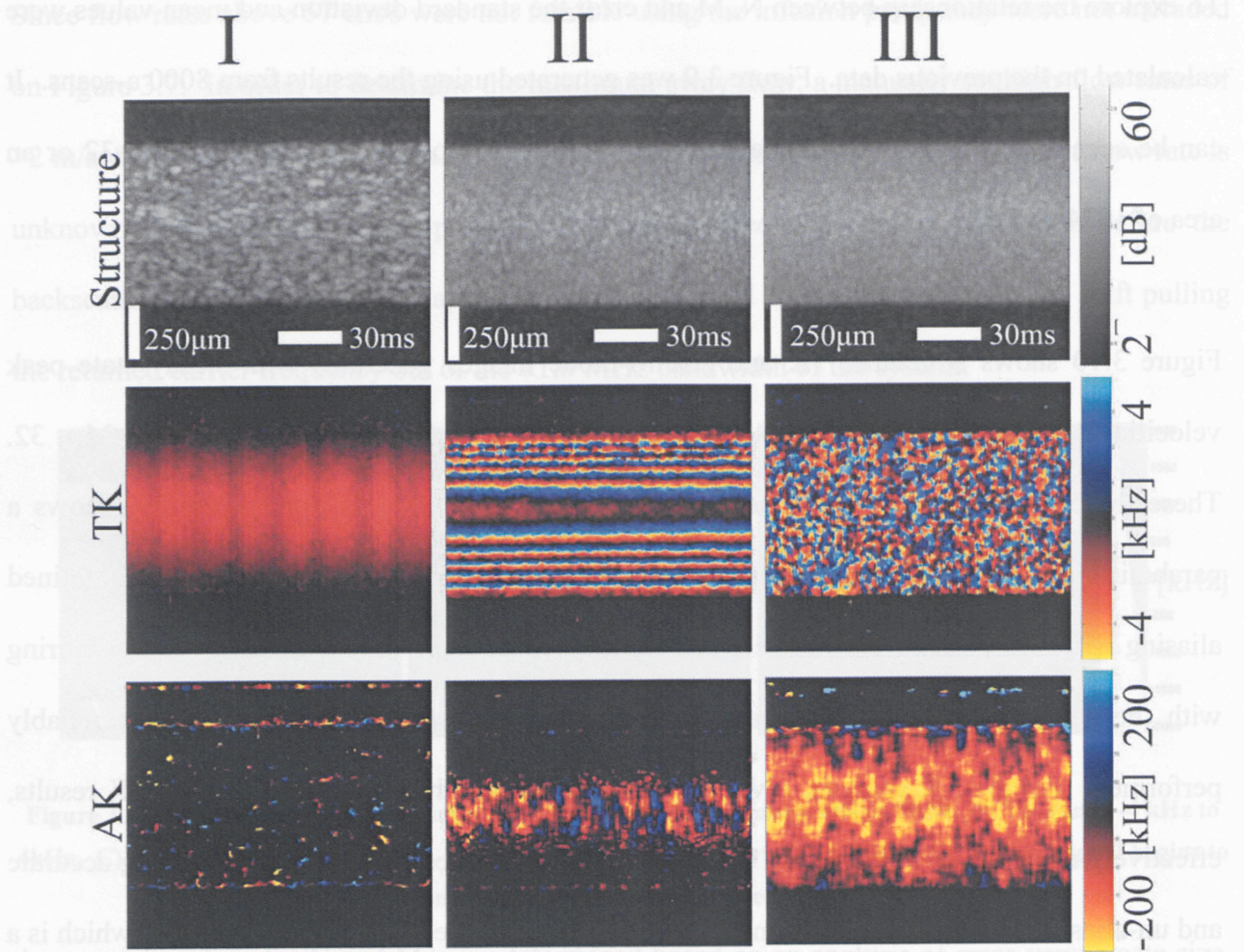


Figure 3.10 - M-mode images of the three detection zones showing structural, AK and TK renderings. In zone I, TK accurately measures velocity, and the aliasing rings in zone II can be unwrapped reliably. In zone III, the aliasing rings on the TK are smaller than the spatial resolution of the system and can not be accurately unwrapped. The AK is able to accurately measure flow in zone III, but not in zones I and II.

Finally, to verify that there is a direct correlation which matches based on different angles, a constant flow was analyzed using the AK at two different angles. As seen in Figure 3.11, after correction for angle, refraction and a background subtraction was performed - both velocity profiles closely matched each other peak velocities occurring at ~ 10 cm/s.

Figure 3.9 - Contour map of error versus a change in N and M. N=M=32 is highlighted.

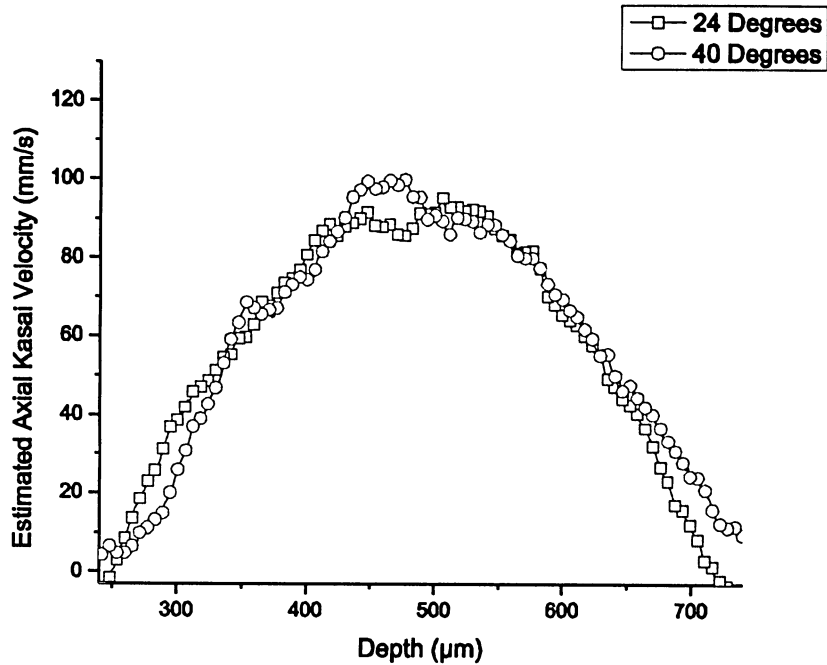


Figure 3.11 – AK velocity estimation for two different angles. Estimation corrected for refraction and angle.

3.3 Experiment 3 – *in vivo* Animal Experimentation

In vivo trans-esophageal M-mode images of a rat aorta were analyzed using the algorithms developed. Experiments were performed using an endoscopic catheter [16] on male Fischer rats. The average body weight was ~180 grams and they were anesthetized with 80 mg/kg of ketamine and 13 mg/kg of xylazine intramuscularly. To avoid food debris in the esophagus, the animals received only water for the day before imaging. During the procedure, the body temperature was monitored and controlled with a heating pad. These procedures were performed in accordance with an institutionally approved animal utilization protocol. The endoscopic DOCT (EDOCT) setup placed the OCT probe into a catheter. The catheter was driven externally as seen in Figure 3.12B.

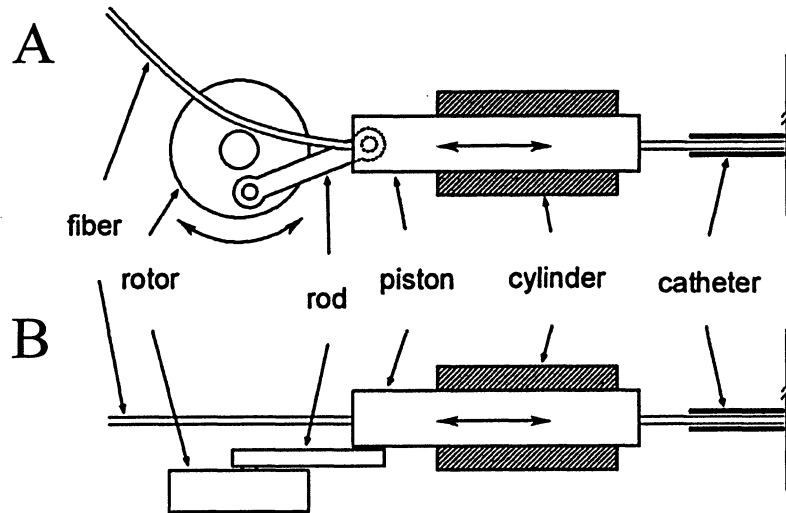


Figure 3.12 –Schematics of the mechanical assembly for the linear scanning catheter, courtesy of Victor Yang. A) Top-view. B) Side-view.

The fiber was coupled through a lens and a right angle prism to image the esophagus at an 82° angle. The prism setup and scanning mechanisms are shown in Figure 3.13.

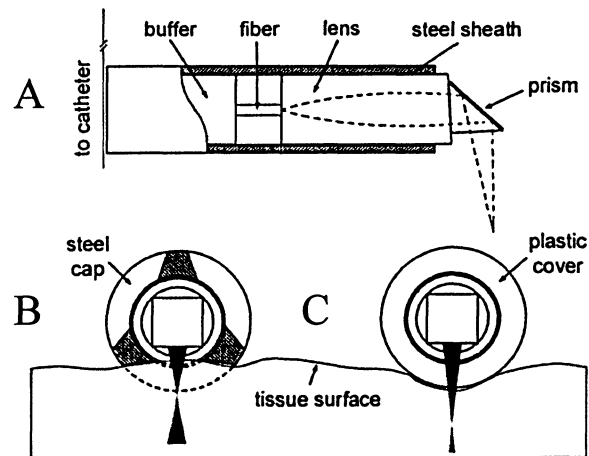


Figure 3.13 – Schematic of the EDOCT catheter distal end, courtesy of Victor Yang. A) Fiber termination with a GRIN lens and right angle prism. The terminated fiber can slide within either a steel cap, with the optical beam passing through one of the slots B) or within a transparent plastic cover seen in C).

Data collected were processed using both structural image processing, as well as the TK and AK Doppler variants. Figure 3.14A shows the structural image with the overlaid TK estimated Doppler frequency, while in Figure 3.14B, the same structural image is overlaid with the AK results after background frequency subtraction. The rat heart rate was measured to be 230 beats per minute or 0.26 s per beat. A temporal smoothing filter set at 0.025 s in length ($< 10\%$ of the cardiac cycle), was used to improve the SNR while still preserving the temporal resolution and allowing visualization of the cardiac cycle. The Doppler angle was approximately 82° . The peak systolic velocity through the aorta was estimated to be ~ 1 m/s (Figure 3.14C), in good agreement with values found in literature [6]. Comparing Figures 4A and 4B, it is evident that the TK is sensitive to a slower flow, detecting the pulsating motion of the aortic wall (velocity < 2 mm/s), while the AK is capable of estimating high flow velocities (> 1 m/s) without aliasing using the same data set.

To the best of our knowledge, the peak systolic velocity through the aorta of ~ 1 m/s, as seen in Figure 3.14C, is the highest *in vivo* flow rate measured by OCT or any of the current Doppler variants. Careful inspection of Figure 3.14A shows that the sensitivity of the TK is able to detect even the pulsating motion of the aortic wall as blood is pumped through the vessel. The TK is also sensitive to regions of slow flow. When compared to Figure 3.14C, one can appreciate that the AK is capable of visualizing extremely high flow velocity without aliasing artifacts in regions where the TK is aliased beyond unwrapping techniques.

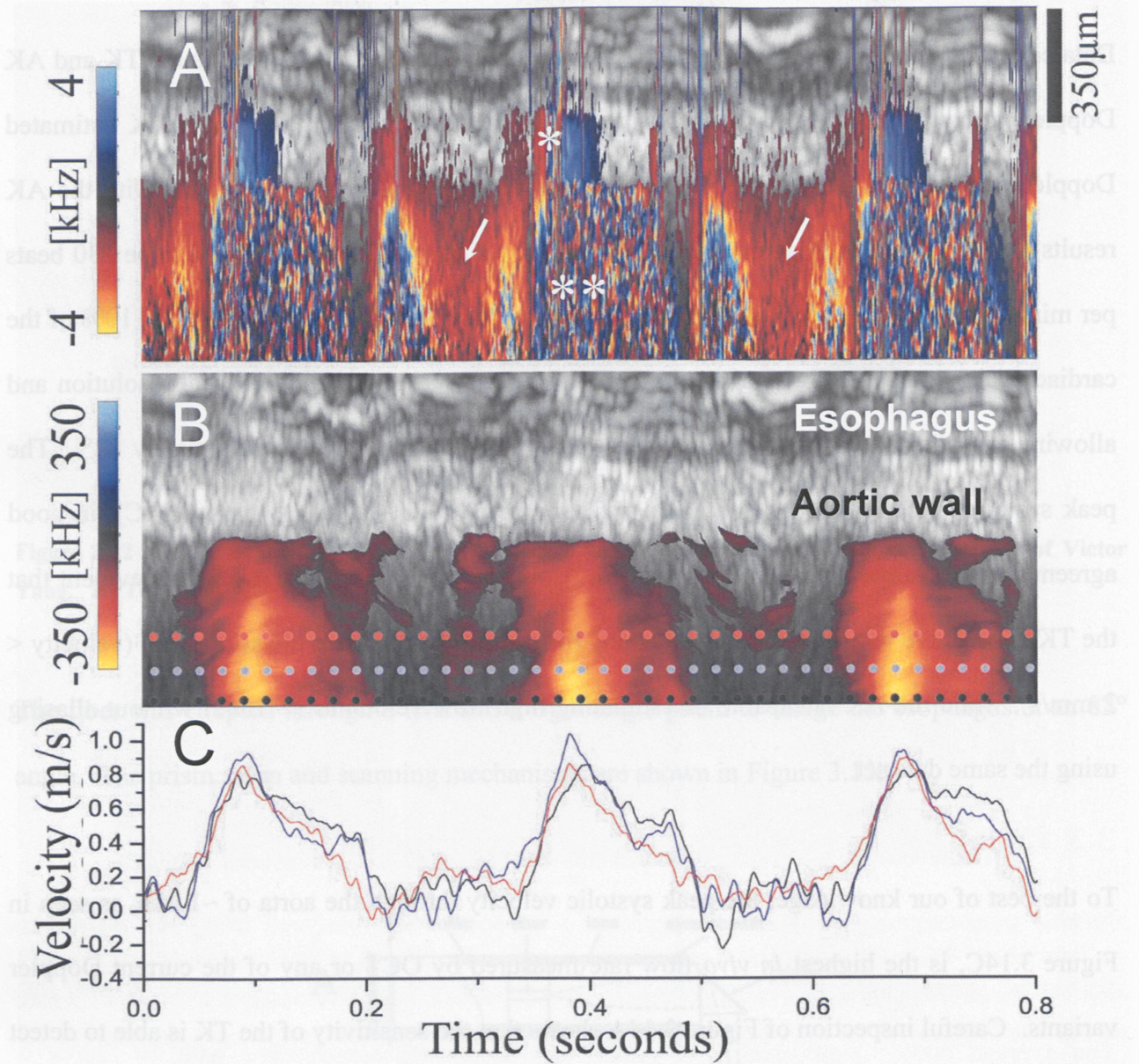


Figure 3.14 – *In-vivo* images of trans-esophageal Doppler OCT of rat aortic blood flow. (A) TK results overlaid on structural image. Doppler signals indicate aortic wall motion (*), systolic rush of high-speed blood flow (**), and regions of slow flow between heart beats (white arrows). (B) AK results overlaid on the same structural image, with the esophagus and aortic wall labelled. High speed systolic flow regions consistent with large Doppler frequency shifts are clearly visualized. The temporal flow profiles measured at the dotted lines of corresponding colors in (B) are plotted in (C).

Figure 3.13 – Schematic of the EDOCT catheter distal end, courtesy of Victor Yang. A) Fiber termination with a GRIN lens and right angle prism. The terminated fiber can slide within either a steel cap, with the optical beam passing through one of the slots B) or within a transparent plastic cover seen in C).

4 Chapter 4: Conclusion

The experimental setup demonstrated that the AK algorithm was able to detect a change in the backscattered mean carrier frequency based on the motion of the scattering object. Due to phase instability in the OCT system that was used, the minimum detectable frequency shift was fairly large when compared to the detectable shift using the TK. However, through careful analysis of the data, it was demonstrated that the TK and AK results overlap if phase unwrapping is performed on the TK. Through a combination of the TK, TK with unwrapping and AK on the same data set, velocities from 10 $\mu\text{m/s}$ to 1.5 m/s were resolved. The previous un-aliased maximum velocity detection on this OCT system was 4 mm/s , so the combination of unwrapping and AK estimation has increased flow estimation by $\sim 400\times$.

The AK was further verified through use in an *in vivo* application. By imaging the aorta of a rat through the esophagus, it was demonstrated that a peak flow velocity of $\sim 1 \text{ m/s}$ can be obtained when imaging at a Doppler angle of 82° . The TK was able to detect the small movement in the aortic wall and periods of low flow while the AK demonstrated detection of the high speed systolic rushes.

Through experimental and *in vivo* results, the AK has proven to be a viable method for detecting high flow rates using interferometric data. The combination of TK, TK with unwrapping and AK can now be used to image flow rates ranging from microcirculation rates to coronary applications. At the time of the submission of this thesis, work has been accepted to the 2006 SPIE Photonics West conference. Additionally, an Optics Letters publication is undergoing peer review and is patent pending.

4.1 Future Work

This data was obtained and processed using a time-domain phase OCT system. Swept source Fourier domain OCT systems are able to image at much higher frame rates over time-domain systems. A feasibility study can be performed to see if the AK is compatible with the scanning mechanisms utilized by the swept source OCT systems. If the AK algorithm is compatible, then the higher frame rates and increased SNR will allow even better velocity estimation.

The Mayo Clinic, a well known American non-profit medical practice, has expressed an interest in obtaining an OCT system with the TK/AK algorithm for clinical diagnosis. A real-time, 32FPS application would be developed using a combination of field programmable grid array (FPGA) and PC hardware with National Instruments LabView. Cardiac models can be tested *in vivo* with intravascular experiments on pigs to determine feasibility at higher flow rates. Other areas that the algorithms developed can be utilized in are radial scanning of intraluminal flow at high velocities and cerebral arteriolar flow measurement.

Backscattered effects, arising from scatterer size, cause effects such as the sky appearing blue. Since OCT is a light based system, there will be some type of spectroscopic effect involved with the backscatter of the photons. These applications have not yet been determined. In itself, that is a large project. Potential non-linear effects are generated by the motion of the RSOD. To avoid these effects, the scanning can be stopped and data collected at a specific depth over time. This data is expected to again verify that the real Doppler signal is being obtained. If the spectroscopic data accurately predicts scatterer size, some potential applications would be the early detection of cancerous cells by calculating nucleus size change, detection of apoptosis and

macrophage infiltration of the lipid pool under the plaque. Preliminary data suggests that there is a spectroscopic change related to the size of the scatterer.

Different sized scattering objects were imaged to see if there was a change in the background frequency information based on scatterer size. Intralipid solution, which has a mean particulate size of $\sim 100\text{nm} \pm 10\text{nm}$, should cause a Rayleigh scattering effect based on the 1300 nm wavelength of the laser. Stationary Intralipid solution in a Petri dish was imaged. This procedure was then repeated using silicon beads with a diameter of 1 μm . The silicon beads were dissolved in water, insonified, separated with a centrifuge and then insonified again before imaging to get a uniform distribution. Comparison between these two results seems to demonstrate that there is in fact a different back-scattered mean frequency related to scatterer size. The Intralipid has a higher backscattered mean frequency at low depths, but as the depth increases the mean frequency reduces. This appears consistent with the Rayleigh scattering as the lower wavelength components are more strongly reflected with a preference of $1/\lambda^4$.

Investigating this effect with a data set from the *in-vivo* experimentation seems to demonstrate that there is a frequency change between different layers of the esophagus. These effects have not yet been analyzed and are being presented for future reference.

4.2 Funding

Support from the Canada Research Chairs program, Ontario Centres of Excellence through the Photonics Research Ontario program, and Canadian Institutes of Health Research are gratefully acknowledged.

References

- [1] D. Huang, E.A.Swanson, C.P.Lin, J. S. Schuman, W. G. Stinson, W. Chang, M. R. Hee, T. Flotte, K. Gregory, C. A. Puliafito, and J. G. Fujimoto, "Optical coherence tomography," *Science*, vol. 254, pp. 1178-1181, 1991.
- [2] C. Kasai, K. Namekawa, A. Koyano, and R. Omoto, "Real-Time Two-Dimensional Blood Flow Imaging Using an Autocorrelation Technique," *IEEE Transactions on Ultrasonics*, vol. SU-32, pp. 458-464, 1985.
- [3] http://en.wikipedia.org/wiki/Electron_microscope, "Electron Microscope," 2006.
- [4] http://www.lixi.com/xray_history.htm, 2006.
- [5] <http://www.worldinvisible.com/apologet/humbody/bloodcir.htm>, "Human Blood Circulation," 2006.
- [6] A. B. Driss, J. Benessiano, P. Poitevin, B. I. Levy, and J. B. Michel, "Arterial expansive remodeling induced by high flow rates," *American Journal of Physiology - Heart and Circulatory Physiology*, vol. 272, pp. 851-858, 1997.
- [7] J. A. Jensen, *Estimation of Blood Velocities Using Ultrasound, A Signal Processing Approach*: Cambridge University Press, 1997.
- [8] R. A. Serway, R. J. Beichner, and J. W. Jewett, *Phyiscis for Scientists and Engineers with Modern Physics, Fifth Eddition*: Harcourt, 1999.
- [9] B. E. Bouma and G. J. Tearney, *The Handbook of Optical Coherence Tomography*. New York: Marcel Dekker, Inc., 2001.
- [10] V. X. D. Yang, "Endoscopic Doppler Optical Coherence Tomography," in *PhD Thesis - University of Toronto*, 2004.
- [11] M. L. Gordon, V. X. D. Yang, A. Mok, and I. A. Vitkin, "Analysis of the Optical Delay Generator for Rapid Depth Scanning in Optical Coherence Tomography," 2004.
- [12] K. Qian and S. H. S. A. Asundi, "A simple phase unwrapping approach based on filtering by windowed Fourier transform," *Optics & Laser Technology*, vol. 37, pp. 458-462, 2005.
- [13] A. W. Sainter, T. A. King, and M. R. Dickinson, "Effect of target biological tissue and choice of light source on penetration depth and resolution in optical coherence tomography," *Journal of Biomedical Optics*, vol. 9, pp. 193-199, 2004.
- [14] V. X. D. Yang, M. Gordon, B. Qi, J. Pekar, S. Lo, E. Seng-Yue, A. Mok, B. Wilson, and I. A. Vitkin, "High speed, wide velocity dynamic range Doppler optical coherence tomography (Part I): System design, signal processing, and performance," *Optics Express*, vol. 11, pp. 794-809, 2003.
- [15] V. X. D. Yang, M. Gordon, E. Seng-Yue, S. Lo, B. Qi, J. Pekar, A. Mok, B. Wilson, and I. A. Vitkin, "High speed, wide velocity dynamic range Doppler optical coherence tomography (Part II): Imaging in vivo cardiac dynamics of *Xenopus laevis*," *Optics Express*, vol. 11, pp. 1650-1658, 2003.
- [16] V. X. D. Yang, M. Gordon, S.-j. Tang, N. Marcon, G. Gardiner, B. Qi, S. Bisland, E. Seng-Yue, S. Lo, J. Pekar, B. Wilson, and I. A. Vitkin, "High speed, wide velocity dynamic range Doppler optical coherence tomography (Part III): in vivo

- endoscopic imaging of blood flow in the rat and human gastrointestinal tracts," *Optics Express*, vol. 11, pp. 2146-2424, 2003.
- [17] V. X. D. Yang, M. L. Gordon, A. Mok, Y. Zhao, Z. Chen, R. Cobbold, B. C. Wilson, and I. A. Vitkin, "Application of the Kasai Velocity Estimator and Histogram Segmentation for Resolution Improvement and Motion Suppression in Phase-resolved Optical Doppler Tomography," *Optics Communication*, vol. 209-214, 2002.
 - [18] T. Loupas, J. T. Powers, and R. W. Gill, "An axial velocity estimator for ultrasound blood flow imaging, based on a full evaluation of the Doppler equation by means of a two-dimensional autocorrelation approach," *IEEE Transactions on Ultrasonics, Ferroelectrics, and Frequency Control* vol. 42, pp. 672-688, 1995.
 - [19] G. F. Pinton, J. J. Dahl, and G. E. Trahey., "Rapid tracking of small displacements with ultrasound," *IEEE Transactions on Ultrasonics, Ferroelectrics, and Frequency Control*, vol. 53, pp. 1103-1117, 2006.
 - [20] R. Leitgeb, W. Drexler, A. Unterhuber, B. Hermann, T. Bajraszewski, T. Le, A. Stingl, and A. Fercher, "Ultrahigh resolution Fourier domain optical coherence tomography," *Optics Express*, vol. 12, pp. 2156-2165, 2004.
 - [21] J. A. Izatt, M. D. Kulkarni, S. Yazdanfar, J. K. Barton, and J. Welch, "In vivo bidirectional color Doppler flow imaging of picoliter blood volumes using optical coherence tomography," *Optics Letters*, vol. 22, pp. 1439-1441, 1997.
 - [22] Y. Zhao, Z. Chen, C. Saxer, S. Xiang, J. F. d. Boer, and J. S. Nelson, "Phase-resolved optical coherence tomography and optical Doppler tomography for imaging blood flow in human skin with fast scanning speed and high velocity sensitivity," *Optics Letters*, vol. 25, pp. 114-116, 2000.
 - [23] A. Rollins, S. Yazdanfar, M. Kulkarni, R. Ung-Arunyawee, and J. Izatt, "In vivo video rate optical coherence tomography," *Optics Express*, vol. 3, pp. 219-229, 1998.
 - [24] V. Westphal, S. Yazdanfar, A. M. Rollins, and J. A. Izatt, "Real-time, high velocity-resolution color Doppler optical coherence tomography," *Optics Letters*, vol. 27, pp. 34-36, 2002.
 - [25] C. Deane, "Doppler ultrasound: Principles and practice," September 13, 2006, pp. http://www.centrus.com.br/DiplomaFMF/SeriesFMF/doppler/capitulos-html/chapter_01.htm.
 - [26] Z. Chen, T. E. Milner, D. Dave, and J. S. Nelson, "Optical Doppler tomographic imaging of fluid flow velocity in highly scattering media," *Optics Letters*, vol. 22, pp. 64-66, 1997.
 - [27] X. Li, T. H. Ko, and J. G. Fujimoto, "Intraluminal fiber-optic Doppler imaging catheter for structural and functional optical coherence tomography," *Optics Letters*, vol. 26, pp. 1906-1908, 2001.
 - [28] A. M. Rollins, S. Yazdanfar, J. K. Barton, and J. A. Izatt, "Real-time in vivo color Doppler optical coherence tomography," *Journal of Biomedical Optics*, vol. 7, pp. 123-129, 2002.
 - [29] A. W. Schaefer, J. J. Reynolds, D. L. Marks, and S. A. Boppart, "Real-Time Digital Signal Processing-Based Optical Coherence Tomography and Doppler Optical Coherence Tomography," *IEEE Journal on Biomedical Engineering*, vol. 51, pp. 186-190, 2004.

B List of Symbols

$\Delta\lambda$ – bandwidth of the light (60 nm)

$\Delta\phi$ – change in phase

Δf – change in frequency

Δx – transverse resolution

$\Phi(t)$ – phase estimate from in-phase and quadrature components

Φ_c – phase component of carrier frequency

Φ_f – phase component of forward frequency

Φ_r – phase component of reverse frequency

$\hat{r}(m, n)$ – array of size $m \times n$

$\hat{\gamma}(m', n')$ – autocorrelation of an array

λ – wavelength

λ_o – wavelength of light (1.3 μm)

μ – viscosity

ρ – density

Γ – signal

$\hat{\Gamma}$ – inverse Fourier transform of the autocorrelation function

A – cross-sectional area

A – amplitude of carrier signal

B_r – amplitude of reverse signal

B_f – amplitude of forward signal

c – speed of sound

c – speed of light

d – spot size

f – frequency

f – focal length

f_{1D} – 1-dimensional Kasai Doppler frequency estimation

f_a – axial scanning frequency (8kHz)

f_{AK} – axial Kasai estimate of mean backscattered carrier frequency

$f_{AKstationary}$ – axial Kasai frequency estimate for stationary scatterer

$f_{AKmoving}$ – axial Kasai frequency estimate for moving scatterer

f_c – carrier frequency

f_D – Doppler frequency

f_{dem} – demodulation frequency used in ultrasound system

f_f – induced forward frequency

f_o – original frequency

f_r – induced reverse frequency

f_{TK} – transverse Kasai Doppler frequency estimation

I – in-phase demodulated component of the signal

I_{MAX} – maximum fringe intensity

I_{MIN} – minimum fringe intensity

l – characteristic length

l_c – coherence length

M – number of axial points used for average

m – current axial point

N – number of transverse points used for average

n – index of refraction

n – current transverse point

n_t – index of refraction of tissue (~ 1.4)

Q – quadrature demodulated component of the signal

r – radial position

R – radius

t – time

t_s – time between adjacent depth samples in ultrasound

T_s – pulse repetition in ultrasound systems

T_s – time between samples

v_{2D} – velocity estimation proposed by Loupas

v – velocity

\bar{v} – mean velocity

v_o – peak centre velocity

v_{rel} – relative velocity between emitter and reciever

$z - z_o$ – change in reference length

$2z_r$ – usable region of focus

⑤ 12-85-87